Edinburgh Research Explorer

Evidence for a composite organic–inorganic fabric of belemnite rostra

Corresponding Author: Dr. Rene Hoffmann,

Corresponding Author's Institution: Ruhr Universität Bochum

First Author: Rene Hoffmann

Order of Authors: Rene Hoffmann; D. K. Richter; R. D. Neuser; N. Jöns;
Linzmeier B. J.; R. E. Lemanis; F. Fusseis; X. Xiao; A. Immenhauser

Abstract: Carbonate skeletons of fossil marine organisms are widely used
to reconstruct palaeoceanographic parameters. Specifically, the
geochemistry of Jurassic and Cretaceous belemnite rostra is traditionally
interpreted to represent near sea-surface seawater properties. More
recently, an increasing number of workers, have reported significant
scatter in geochemical data (e.g., δ18O, δ13C, element/Ca ratio) when
comparing rostra from the same stratigraphic level or within a single
belemnite rostrum. This scatter is not explained by differential
diagenetic overprint alone. Here we report petrographic evidence on the
primary ultrastructure of rostra of Megateuthis (Middle Jurassic) and
Belemnitella and Gonioteuthis (Late Cretaceous). The biogenic
ultrastructure consists of a filigree framework of triaxial branches and
tetrahedrons of variable size forming a honeycomb-like network. Data
presented here suggest that these rostra yielded as much as 50 to 90%
primary pore space. On the level of a working hypothesis - and in analogy
with modern cephalopods - we propose that the pore space was formerly
filled with body fluid and/or organic compounds during the life time of
these organisms. Intra-rostral porosity was post mortem occluded by
earliest diagenetic isopachous calcite cements of a non-biogenic origin.
These may have been precipitated due to increased alkalinity related to
the decay of organic matter. If this holds true, then the resulting
fabric represents a composite biogenic/abiogenic structure. In order to
optically separate the two calcite phases forming a single calcite fibre,
we employed a wide range of state-of-the-art analytical tools to thin
sections and ultra-thin sections of well-preserved specimens. Pending a
verification of these well-supported ultrastructural data by means of
high-resolution geochemical analyses from biogenic and abiogenic phases,
we suggest that these findings have significance for those using
belemnite rostra as archives of their palaeoenvironment.

Dr. René Hoffmann
Ruhr Universität Bochum
Department of Earth Sciences
Institute of Geology, Mineralogy, and Geophysics
Branch Paleontology
Universitätsstrasse 150, Building NA2/132
44801 Bochum
Germany
E-Mail: Rene.Hoffmann@rub.de

Bochum 2016-05-30

Dear Editor,

We greatly appreciate the input from two expert reviewers and have implemented the (minor) comments (see revision notes) in nearly all cases. Where we decided to not follow the reviewer's advice, we argue why we do so.

Thank you for your professional work!

Kind regards,

R. Hoffmann on behalf of the authors

Revision Notes

Dear Editor,

We greatly appreciate the input from two expert reviewers and have implemented the (minor) comments in nearly all cases. Where we decided to not follow the reviewer's advice, we argue why we do so.

General: We have included line numbering. Changed text passages are given in italics.

Reviewer SEDGEO5702_revDF – Reviewer 1

Comments made directly in the manuscript:

Line 94:

Belemnite rostra are traditionally considered to secrete their endoskeleton in oxygen isotope equilibrium with ambient seawater...

Belemnites are traditionally considered to secrete their endoskeleton in oxygen isotope equilibrium with ambient seawater...

Comment: We agree with the reviewer, not the belemnite rostra secrete their endoskeleton but the belemnite animal.

Line 127:

Thin sections (30 µm) and ultra thin sections (< 10 µm) of two well-preserved specimens of *Megateuthis gigantea...*

Thin sections (30 µm) and ultra thin sections (< 10 µm) of two well-preserved orthorostra of *Megateuthis gigantea...*

Comment: We agree with the reviewer that it is useful to distinguish between the orthorostrum and the epirostrum, both are present in *Megateuthis*.

Line 317-318:

Referring to the high porosity observed in both belemnite rostra and sepiid cuttlebone it is important to note that these structures are not homologous (Fuchs 2012).

Comment: We agree with the reviewer and added one sentence pointing out that the belemnite orthorostrum and the sepiid cuttlebone are not homologue structures. See below.

Line 334:

Apical region

Apical line region

Comment: We agree with the reviewer that it is better to refer to the apical line region connecting all apical regions during ontogeny instead of the apical region.

Line 359:

...outside of (i.e., the belemnite animal itself)...

... outside of the orthorostrum (i.e., the belemnite animal itself)...

Line 424:

shell

cuttlebone

Comment: To avoid further confusion between the belemnite rostrum and the tiny rostrum or apical spine at the posterior end of the sepiid cuttlebone, we used the general term cuttlebone for the latter which includes the highly porous phragmocone (see below).

Line 425:

...belemnite skeleton...

...belemnite orthorostrum...

Comment: As pointed out earlier by the reviewer it is more precise to refer to the orthorostrum instead of the whole belemnite skeleton which would include the phragmocone as well – which has a different mineralogy and ultrastructure and was not analysed in this study.

Line 428:

...living belemnites...

...living belemnite rostra

Comment: Changes accordingly to the comment by the reviewer.

Line 434:

...ommastrephid...

...*onychoteuthid*...

Comment: We changed the text accordingly to the comment by the reviewer.

Line 495:

Reviewer question: Does this concentration refers to the entire cuttlebone or only the sepiid spine ("rostrum")?

Comment: All cited references refer to the *Sepia* cuttlebone and do not specify a particular region, e.g., the spine.

Lines 518-521:

This tentative interpretation presented here with regard to belemnite rostra is arguably consistent with observations of 10-40% organic matrix in the *Sepia* cuttlebone (Birchall and Thomas, 1983; Florek et al., 2009). This is relevant as we suggest that the belemnite rostrum is structurally similar to the *Sepia* cuttlebone with regard to the primary intra-skeletal porosity.

This tentative interpretation presented here with regard to belemnite rostra is arguably consistent with observations of 10-40% organic matrix in the Sepia cuttlebone (Birchall and Thomas, 1983; Florek et al., 2009). This is relevant as we suggest that the belemnite rostrum is structurally similar but not homologous (Fuchs 2012) to the Sepia cuttlebone with regard to the primary intra-skeletal porosity.

Comment: The reviewer suggested to highlight here that the rostrum and sepiid cuttlebone are structurally similar, but not homologous. Accordingly, we added "but not homologous" to the text citing the work of Fuchs (2012). However, a discussion about the similarities and differences of the sepiid and belemnite rostrum is far beyond the scope of this paper.

Comments to the authors:

Reviewer #1: Dear authors, in some places, you compare the belemnite rostrum with sepiid cuttlebones. I recommend to provide a short explanation about the homologous shell parts of belemnites & sepiids. A clear differentiation between rostrum & phragmocone is essential to correctly interpret/comprehend observed porosities. In this context, it would be less confusing to compare the belemnite rostrum with the "rostrum" of sepiids and belosepiids (rather than their phragmocone).

Comment: We agree with the reviewer that the comparison of a belemnite rostrum with the Sepia cuttlebone might be misleading when it comes to the phylogenetic reconstruction of coleoid evolution. However, the reconstruction of coleoid phylogeny is far beyond the scope of our paper. Further, it should be noted that there is an open discussion about the homologous shell parts in fossil and modern coleoids and that authors cited in our manuscript did not distinguish between the different shell parts, e.g., Florek et al. 2009 reported on the amount of organic matter for the whole cuttlebone and did not distinguish between phragmocone, dorsal shield, and rostrum. In order to avoid additional confusion we decide to keep the comparison between the belemnite orthorostrum and the Sepia cuttlebone (which refers to the complete internal shell). We do so specifically because earlier authors, when describing porosity observed in belemnite rostra, compared it with the porous structure of the Sepia cuttlebone not distinguished between the phragmocone and other shell parts. For the "rostrum-problem" the reader is referred to Fuchs (2012). As far as we know no detailed description of the sepiid rostrum is available.

Apart from this, I would avoid the term "skeleton"; if then only in terms of the entire shell; not only shell parts, e.g. the rostrum.

We agree with the reviewer and delete whenever it seemed adequate the term skeleton.

I´m missing a paragraph discussing and verifying earlier observations/ ideas: who postulated a low porosity and what was wrong in the line argumentation?

We provide information about earlier observations of pore space or the varying amount of organic matter in belemnite orthorostra in the introduction part (lines 84-92) and in chapter 4.3 citing the most important articles by Müller-Stoll, Spaeth, and Saelen. Müller-Stoll (1936) argues for varying amounts of organic matter in the observed lighter/darker concentric rings, while Spaeth (1971, 1973, 1975) was the first who described a higher amount of porosity (up to 20%). In his extensive review Saelen (1989) comes to the conclusion that it is most likely that the belemnite rostrum was a dense structure already during life time of the belemnite animal. The latter statement (Saelen 1989) agrees with the majority of contemporaneous and all subsequent researchers (e.g., Veizer 1974, Podlaha et al. 1998) largely neglecting the porosity in belemnite rostra. Maybe this was due to the fact that Spaeth could only present data for a single belemnite rostrum (Neohibolites). To keep the focus on our description of the new ultrastructure and to avoid duplication we do not provide an additional paragraph discussing and verifying earlier observations dealing with the belemnite porosity.

Reviewer SEDGEO5702 Review 27 April 2016 IJ comments – Reviewer 2

All minor corrections were implemented in the revised version of the manuscript.

Line 275:

Reviewer question: Why specifically choose these elements for mapping? Common substitutions in the calcite lattice such as Sr, Ba, Fe, Mn, Zn are not mentioned. Do these not show any variation?

Comment: Fe, Mn content was quantitatively assessed using the cathodoluminescence microscope. Both show slight variation between the biogenic precipitates and secondary cement phases. We

specifically choose Mg, P, and S to collect arguments for the distribution of primary organic matter as we discussed in our manuscript.

Line 355:

... the dense fabrics observed in the case of most rostra collected in Mesozoic sedimentary successions...

... the dense fabrics observed in rostra collected in Mesozoic sedimentary successions...

Comment: We agree with the reviewer that it is surprising that no examples of preserved pore space exist as far as we know. However, fossil echinoderm remains, with a primary comparable porous endoskeleton, are also preserved as massive fossil structures with nearly no pore space left. Some belemnite rostra are preserved as hollow tubes thanks to strong diagenetic alteration processes. In some cases the outer margin of belemnite orthorostra show increasing porosity. This porosity is taken as sign of diagenetic alteration and does not resemble the described ultrastructure.

Line 384:

Reviewer statement: Yet echinoderm calcite commonly retains its intraparticle porosity in geological samples, despite being Mg-calcite!

Comment. We do not agree with the reviewers statement. Based on our own observations the majority of the primary pore space in echinoderm skeletons is occluded by secondary calcite (see also Dickson 2001, 2002, 2004). However, due to staining it is possible to reveal the original skeletal structure and distinguish it from the secondary cement phase.

Line 510:

Reviewer question: Are there any examples of cuttlebone being preserved in the way that you propose for belemnites?

Comment. As far as we know the ultrastructure of fossil sepiid cuttlebones is not described in comparable details. Further, no taphonomic framework for fossil cuttlebones is available.

Comments to the authors:

Reviewer #2: (1) The authors state (p14) that "The presence of a highly porous primary rostrum architecture during the life time of the belemnite organism as proposed here, is contrasted by the dense fabrics observed in the case of most rostra collected in Mesozoic sedimentary successions (Fig. 1A-B)."

They state "most", implying that not all belemnites have dense fabrics? I find it rather surprising that if their hypothesis is correct, why no examples of preserved porous calcite guards have ever been found. Is there any evidence of the existence of these, perhaps having been dismissed as 'altered' or 'leached' specimens? Such material would lend strong support to your hypothesis.

Comment. We agree with the reviewer that it is surprising that no examples of preserved pore space exist as far as we know. We have collected belemnite rostra from many different localities (Russia, Japan) while the primary intention was to collected hollow ammonites. Hollow ammonite preservation is very rare and requires special conditions. It can be assumed that belemnites collected from the same beds share a similar unique taphonomy. However, also those belemnite rostra collected together with hollow ammonites show a massive structure. Some belemnite rostra are preserved as hollow tubes thanks to strong diagenetic alteration processes. In some cases the outer margin of belemnite orthorostra show increasing porosity. This porosity is taken as a sign of diagenetic alteration and does not resemble the described ultrastructure. By the observation of darker and lighter concentric rings earlier researchers speculated about varying amounts of organic within these rings. Recently, Ullmann et al. (2015), based on geochemical analyses, postulated a 40% porosity for the apical line region. It was assumed by Ullmann et al. (2015) that the porosity decreases towards the rostral margin. Concluding, as far as we know no pore space had been described so far the fits with the herein described ultrastructure.

(2) The authors refer to the microstructure of echinoderm calcite (p16). They do not mention that echinoderm skeletons are also porous and subject to diagenetic infill. Yet echinoderm calcite may sometimes retain its intraparticle porosity even in Palaeozoic samples, despite originally being Mg-calcite! Why should belemnites be so uniform in their preservation style? A consequence of their unique crystallography?

Comment. We do not agree with the reviewers statement. Based on our own observations the majority of the primary pore space in echinoderm skeletons is occluded by secondary calcite (see also Dickson 2001, 2002, 2004). However, due to staining it is possible to reveal the original skeletal structure and distinguish it from the secondary cement phase.

(3) Cuttlebone is presented as the closest modern analogue to belemnite guards (e.g. p20). This seems to be perfectly logical. However, again, are there any examples recorded of cuttlebone being preserved in a similar manner to that proposed for belemnites? If the mechanism is valid, it seems rather surprising that no similar processes have been observed / described, even if only in a more superficial way. The different taphonomy a consequence of their aragonite mineralogy perhaps?

Comment. Sepiid cuttlebones are rather rare compared to the globally distributed and highly abundant belemnite rostra. We assume the different preservation originally lies in their different primary mineralogy (low Mg calcite for belemnites and aragonite for sepiids).

Thank you for your professional work!

Kind regards,

R. Hoffmann on behalf of the authors

1 **Evidence for a composite organic-inorganic fabric of belemnite rostra: Implications for palaeoceanography and palaeoecology**

3

4 Hoffmann, R.[1], Richter, D.K.[1], Neuser, R.D.[1], Jöns, N.[1], Linzmeier, B.J.[2], Lemanis, R.E.[1], Fusseis, F.[3], Xiao, X.[4] and Immenhauser A[1]

6

7 [1] Department of Earth Sciences, Institute of Geology, Mineralogy, and Geophysics; Ruhr-Universität Bochum, Universitätsstrasse 150, 44801 Bochum, Germany

9 Corresponding author. E-mail address: rene.hoffmann@rub.de (R. Hoffmann), phone number: +49-234-3227769

11 [2] Department of Geoscience, University of Wisconsin – Madison, 1215 West Dayton St, Madison, Wisconsin, USA

13 [3] School of Geosciences, The University of Edinburgh, Grant Institute, King's Buildings, West Mains Road, Edinburgh, UK EH9 3JW

15 [4] Advanced Photon Source, Argonne National Laboratory, 9700 S. Cass Ave., Lemont, IL, 60439 USA.

16

17

18

19

20

21

22

23

24

25

26

Abstract

Carbonate skeletons of fossil marine organisms are widely used to reconstruct palaeoceanographic parameters. Specifically, the geochemistry of Jurassic and Cretaceous belemnite rostra is traditionally interpreted to represent near sea-surface ~~palaeoenvironmental parameters~~seawater properties. More recently, an increasing number of workers, ~~however, report a~~have reported significant scatter in geochemical data (e.g.~~,~~ δ^{18}O, δ^{13}C, element/Ca ratio) when comparing rostra from the same stratigraphic level or within a single belemnite rostrum. This scatter is not explained by differential diagenetic overprint alone. Here we report petrographic evidence on the primary ultrastructure of rostra of *Megateuthis* (Middle Jurassic) and *Belemnitella* and *Gonioteuthis* (Late Cretaceous). The biogenic ultrastructure consists of a filigree framework of triaxial branches and tetrahedrons of variable size forming a honeycomb-like network. Data presented here suggest that these rostra yielded as much as 50 to 90% primary pore space. On the level of a working hypothesis - and in analogy with ~~Recent~~modern cephalopods - we propose that the pore space was formerly filled with body fluid and/or organic compounds during the life time of these organisms. Intra-~~skeleton~~rostral porosity was post mortem occluded by earliest diagenetic isopachous calcite cements of a non-biogenic origin. These may have been precipitated due to increased alkalinity related to the decay of organic matter. If this holds true, then the resulting fabric represents a composite biogenic/abiogenic structure. In order to optically separate the two calcite phases forming a single calcite fibre, we employed a wide range of state-of-the-art analytical tools to thin sections and ultra-thin sections of well-preserved specimens. Pending a verification of these well-supported ultrastructural data by means of high-resolution geochemical analyses from biogenic and abiogenic phases, we suggest that these findings have significance for those using belemnite rostra as archives of their palaeoenvironment.

Keywords: belemnite, ultrastructure, carbonate archive, diagenesis, Jurassic-Cretaceous

1.   Introduction

The ultrastructure of recent biogenic carbonates is of great interest for those concerned with biomineralization research in general (Weiner and Addadi, 2011; Goetz et al., 2011), those studying the primary biogenic skeletal structures of fossil skeletal hardparts (e.g., Coronado et al., 2013), and for palaeoceanographers exploring these materials for their bearing on past climate dynamics (Saelen, 1989; Cochran et al., 2003; Parkinson et al., 2005; Jarvis et al., 2015; Immenhauser et al., 2016). Whereas the tests of planktonic and benthic foraminifera (and coccoliths etc.) are important archives of open marine environments throughout the Cenozoic and beyond (e.g., Zachos et al., 2001), much of what is known about Cretaceous and Jurassic palaeoceanography has been deduced from the geochemical archive of the calcareous rostra of extinct cephalopods, specifically belemnites (Dutton et al., 2007). Reasons for the wide use of these archive materials include their abundance in the fossil record, the diagenetically stable low-Mg calcite mineralogy of rostra (Veizer, 1974; Saelen, 1989), and the broad palaeobiogeographic distribution of belemnites in the marine Boreal and Tethyan realms, (e.g., Urey Urey et al., 1951; Voigt et al., 2003; Wierzbowski, 2004; McArthur et al., 2007; Dutton, 2007; Price and Page, 2008; Wierzbowski and Joachimski, 2009; Price et al., 2009 2011; Li et al., 2012, 2013). As with all biogenic carbonates, however, these archives undergo post- mortem diagenetic alteration, representing a major obstacle in carbonate research (Swart, 2015).

Characteristic geochemical patterns and fabrics in biogenic carbonate hardparts have been used to test for example molluscks (e.g., Cochran et al., 2003, Sessa et al., 2015, Immenhauser et al., 2016), brachiopods (Parkinson et al., 2005), or foraminifera (e.g., Huber and Hodell, 1996; Kozdon et al., 2011) for evidence of diagenetic alteration. In the case of ammonites, the degree of preservation of nacre tablets provides evidence with regard to the preservation of these exoskeletons, to name one example (e.g., Cochran et al., 2010). With regard to belemnite rostra, the observation of well-preservedan intact fibrous microfabrics in thin sections and polished rock surfaces in combination with cathodoluminescence is commonly used to identify well- preserved belemnite rostra (Rosales et

al., 2001). In contrast, cloudy areas, exfoliation, fractures, stylolites, or boring traces are interpreted as evidence for post -mortem alteration (Saelen, 1989; Li, 2011; Benito and Reolid, 2012). A rigorous discussion of screening techniques, including trace- element concentrations, and isotopic ratios applied to biogenic low-Mg calcite macrofossils, ishas been provided by Ullmann and Korte (2015). Similarly, a "best practice" approach for the interpretation of mollusc and brachiopod carbonate archives was presented in by Immenhauser et al. (2016).

The ultrastructure of belemnite rostra was first studied by Müller-Stoll (1936). This author described organic-rich (laminae obscura) and carbonate-rich (laminae pellucidae) concentric growth rings. Both of these were later shown to be calcitic but differ due to variable degrees ofamounts of occluded organic matter (Saelen, 1989). Growth rings are made up by fibrous calcite crystals radiating from a central zone called apical line (Richter et al., 2011) forming what seems to be a low-porosity fabric (Saelen, 1989 and references therein; Fig. 1A-C). Single fibres (= radial structures of Saelen, 1989) can be arranged in bundles traversing the concentric growth layers. Each fibre thickens outwards and shows a sub-fibrous framework potentially first proposed - but not further explored - by Saelen (1989, Fig. 15a).

Belemnites rostra are traditionally considered to secrete their endoskeleton in oxygen isotope equilibrium with ambient seawater (e.g., Anderson et al., 1994; Price and Sellwood, 1997; Voigt et al., 2003; Price et al., 2009; Wierzbowski and Joachimski, 2007, 2009). The main argument brought forward is commonly the presence of what are considered cyclical oxygen isotope patterns interpreted as seasonal seawater temperature variations (Urey et al., 1951). The PeeDee belemnite used in Urey´s study was considered as well-preserved based on the compact fabric and the optical features of the calcite crystals (but see Li, 2011 for discussion). The assumption of equilibrium precipitation was further supported by data sets from recent cephalopods including *Nautilus*, *Sepia*, and *Spirula* precipitating their skeletal hardparts in near-equilibrium with $\delta^{18}O_{seawater}$ (Lukeneder et al., 2010). In contrast to this traditional view, there is an increasing amount of evidence suggesting that belemnite rostra are problematic archives of their palaeoenvironment (see Immenhauser et al.,

105   2016 for detailed discussion). For example, Price et al. (2015) reported an offset of about 5℃

106   between the aragonitic phragmocone and the calcitic rostrum of a single specimen of

107   *Cylindroteuthis*. This offset was regarded as vital effect but it remains unclear whether the

108   temperatures derived from the aragonite are too warm or from the calcite too cool. Similarly, high

109   intra-rostral variability of elemental (Ca, Mn, Mg, Fe, Sr) and isotopic (δ^{18}O, δ^{13}C) composition, the

110   latter with a scatter of up to 2‰, has been reported from belemnite rostra lacking evidence for

111   diagenetic alteration (Podlaha et al., 1998).

112   The significant discrepancy of these data sets forms a strong motivation for a reconsideration of

113   belemnite rostra as archives of their palaeoeenvironment. Here, we report data from a wide set of

114   state-of-the-art analytical infrastructure applied to thin- and ultra-thin sections of exceptionally well-

115   preserved Jurassic and Cretaceous belemnite rostra. The following aims guided this paper: First, to

116   present well-constrained petrographic evidence for the complex primary biogenic framework of

117   these rostra; second, to document evidence that points to athe highly porous nature of this biogenic

118   framework; third, to assess the relative proportion between primary skeleton and porosity; fourth, to

119   discuss the timing and nature of the pore-filling calcites phase. Evidence reported here has

120   significance for the interpretation of proxy data from ancient belemnite rostra and forms the

121   foundation of a detailed, high-resolution geochemical study that will be in the focus of forthcoming

122   work.

123

124   **2.   Materials and Methods**

125   *2.1. Belemnites*

126

127   Thin sections (30 μm) and ultra- thin sections (< 10 μm) of two well-preserved ~~specimens~~

128   orthorostra of *Megateuthis gigantea* (Schlotheim, 1820) from the Middle Jurassic~~)~~ and one specimen

129   of *Belemnitella mucronata* (Schlotheim, 1813) and *Gonioteuthis quadrata* (Blainville, 1827) from the

130   Upper Cretaceous~~)~~ were studied. Specimens of *Megateuthis* were collected in Bajocian marly

131   limestone deposits from southern Germany. *Belemnitella* rostra are from the late early Campanian

132   (*mucronata* Zone), and *Gonioteuthis* from the early Campanian *lingua/quadrata* –

133   *gracilis/mucronata* Zone from northwestern Germany. *Gonioteuthis* and *Belemnitella* rostra were

134   embedded in calcareous (65-90%) epicontinental shelf deposits of the Misburg Formation (Niebuhr,

135   1995; Niebuhr et al., 2007). Specimens did not display evidence for exfoliation nor did they show

136   boring traces of the surfaces of rostra. Specimens were sectioned along their long axis in a marginal

137   position and perpendicular to the c-axis of their calcite fibres. One section cuts the rostrum of

138   *Megateuthis* perpendicular to the long axis.

139

140   *2.2. Methods*

141

142   Surfaces of thin sections were chemo-mechanically etched using colloidal silica (OP-S) for 5-15

143   minutes to reduce surface irregularities on an atomic scale (Massonne and Neuser, 2005) and coated

144   by a thin carbon layer. All coated thin sections have been studied under a high-resolution field

145   emission scanning electron microscope (HR-FESEM) type LEO/ZEISS 1530 Gemini using a backscatter

146   detector (BSD) at the Ruhr-Universität Bochum, Germany (Figs. 1-3).

147   Crystallographic orientation of belemnite calcite fibres was determined by electron

148   backscattered diffraction (EBSD; Nordlys, OXFORD Instruments). The data acquisition and analysis

149   was performed using the software packages AZtec and Channel 5 by Oxford Instruments (Fig. 4). The

150   scanning electron microscope (SEM) was operated at beam energy of 20 kV, an aperture of 60 μm, a

151   working distance of 25 mm and a tilt angle of 70°. Thin sections were mapped at Bochum University

152   in the high-resolution mode using a grid matrix (1149x748 points) at a step width of 2.017 μm

153   (Fig. 4A) and (543x266 points) at a step width of 1.652 μm (Fig. 4D) and for the single calcite

154   fibre 50 μm to reduce artefacts and increase the reliability of the data. The orientations of the

155   crystals in the individual maps were visualized using a rainbow colour coding ranging from blue

156   over green and yellow to orange and red, where identical colours indicate identical crystal axis

6

157 orientations. For visualizing the weak angular deviations in the crystal lattice in a single calcite fibre,

158 we applied an angular resolution of 2 degrees for the complete rainbow colour range. In addition,

159 orientations of the measured crystallographic axes awere plotted into the lower hemisphere of a

160 Schmidt net (Fig. 4E).

161 Rostra were further investigated under a cathodoluminescence microscope type HC1-LM by

162 Lumic equipped with a hot cathode (Neuser et al., 1996) and a digital camera system (DP73 by

163 Olympus) for recording digital images at Bochum. Beam energy of 14kV and a beam current density

164 between 5 and 10 µA/mm² were generally used for the CL-measurements. Integration times for CL-

165 spectra were commonly between 10 and 60 seconds (Fig. 5).

166 X-ray element distribution maps were acquired using a Cameca SX5FE field emission electron

167 microprobe at Bochum. The acceleration voltage was 15 keV with a probe current of about 80 nA and

168 a fully focused beam. The intensity of S Kα1 was recorded simultaneously on two wavelength

169 dispersive spectrometers equipped with LPET and PET analyzing crystals. The Mg Kα1 line was also

170 measured on two spectrometers (LTAP and TAP crystals), whereas P Kα1 was measured on a single

171 spectrometer equipped with a LPET crystal. The images were acquired in continuous stage scan

172 mode. They have a resolution of 2048 x 1536 pixel, and the dwell time was 17 ms per pixel (Fig. 6).

173 To test for the distribution of organic matter within the belemnite rostra, thin sections were

174 studied under thea fluorescence microscope (Leica DM4500P) equipped with a mercury short-arc

175 reflector lamp coupled with a Leica EL6000 compact light source. We used the blue light filter set

176 producing bright green fluorescence images (filter set I3 for blue light excitation: excitation 450-490

177 nm, emission 515 nm, voltage 100-240 VAC and 50-60 Hz frequency; Fig. 7). Fluorescence microscopy

178 in the manner applied here is an optical tool to qualitatively document the spatial distribution of

179 organic matter in shells. Fluorescence reflects organic matter and less commonly crystal lattice

180 defects and solid inclusions in crystals. Fuorther more details of this methods have been presented

181 please refer toby Wanamaker et al. (2009) and Ritter et al. (subm.).

182   Confocal laser fluorescence microscopy (CLFM) images on an uncoated *Megateuthis* mount

183   were made using a Bio-Rad MRC-1024 scanning confocal microscope at the W. M. Keck Laboratory

184   for Biological Imaging at UW-Madison (Fig. 8). The microscope was operated with a 40 mW laser at

185   wavelengths of 488 nm, 568 nm, and 647 nm. All three wavelengths were simultaneously rastered

186   across the sample. Naturally occurring compounds within the sample caused fluorescence at multiple

187   wavelengths. Images were collected through the following three emission filters: visible green light (λ

188   = 505 to 539 nm); visible red light (λ = 589 to 621 nm); and far-red light (λ = 664 to 696 nm).

189   In order to analyze the three dimensional filigree framework, synchrotron radiation based

190   micro-computed tomography was applied (Fig. 9). Data were collected at the bending magnet beam

191   line 2-BM at the Advanced Photon Source, Argonne National Laboratory, USA. A double multilayer

192   monochromator of 1.5% band-width provided 27.2 KeV X-rays. Images were collected in transmission

193   mode by a CCD camera behind the sample in the hutch configuration. The sample-detector distance

194   was set to 300 mm to collect quantitative phase contrast data. 1440 projections were acquired while

195   the sample was rotated over 180° in steps of 0.125°. A microtomographic data set with a size of 2048

196   x 2048 x 1948 voxels was reconstructed using a phase retrieval algorithm (Mokso et al., 2013).

197

198

199   **3.   Results**

200   *3.1 Optical-, cathodoluminescence-, fluorescence-, and confocal laser fluorescence microscopy (TL, CL,*

201   *FL, CFLM)*

202   Under transmitted light (TL), thin sections of rostra cut perpendicular to the c-axis of calcite

203   fibres reveal a banded distribution of calcite fibres containing brownish triangular elements of

204   variable size (Fig. 5A, D). Some of the larger fibres contain a triangular, organic-rich centre, with its

205   innermost domains occluded by translucent calcite. Bundling of neighbouring calcite fibres is

206   indicated by their subparallel orientation of their a-axis (Fig. 5D). A uniform extinction (orientation)

8

207 pattern of adjacent fibres under crossed polarizers is observed (Fig. 5B, E) and is in agreement with

208 EBSD data (Fig. 4A). Individual fibres display an undulatory extinction (converging or diverging c-axes)

209 under crossed polarizers. Calcite occluding space between organic-rich elements and fibre

210 reinforcement is translucent and contains little or no organic matter (Fig. 5D). Brownish, triangular

211 elements have a relatively low optical relief, compared to the surrounding translucent calcite with a

212 relatively higher optical relief (supplement Fig. 1A-B).

213   Three different luminescence patterns are observed under the cathodoluminescence

214 microscope (CL): (i) A light blue luminescence of the brownish, triangular elements (Fig. 5C, F); (ii)

215 dark blue, intrinsic luminescence of the translucent phase; (iii) locally, orange to red luminescent

216 fractures and microstylolites are observed. In rare cases, fractures retrace the triangular outline of a

217 fibre (Fig. 5C, F, supplement figure 1D).

218   Brownish triangular areas under transmitted light display light green fluorescence while the

219 translucent areas show a dark green fluorescence under the fluorescence microscope (FL).

220 Microfractures are darker under transmitted light compared to the triangular elements and show a

221 light green fluorescence (Fig. 7A-B).

222   Different fluorescence patterns under the CLFM reveals calcite domains visible in BSE (and

223 other) imaging techniques (Figs. 3, 5-7). Filled cracks fluoresce brightly in green and red wavelengths

224 (Fig. 8B-C). Domains that are dark in BSE do not fluoresce in CLFM (Fig. 8A-D). Bright domains in BSE

225 fluoresce brightly in CLFM at all wavelengths observed (Fig. 8A-D). Higher magnification reveals

226 brighter fluorescence between adjacent domains that appear bright in BSE (Fig. 8D).

227

228 *3.2 Scanning-electron microscopy equipped with a backscatter detector (SEM BSD)*

229   Images collected with the scanning electron microscope equipped with a backscatter detector

230 present important evidence for the presence of two calcite phases (dark and bright) of different

231 chemical compositions building the rostra studied. The brownish triangular areas under transmitted

232 light are dark in BSE. Thin sections cut perpendicular to the c-axis of the radiaxal fibrous calcite (Fig.

233 1D I-IV) reveal a complex framework, dark in BSE, surrounded by relatively brighter calcite (Figs. 1-3).

234 Cross sections of the majority of fibres are polygonal or, less often, honeycomb shaped with a tri-

235 radial (120°) symmetry representing an ultrastructure that has not ~~yet~~ been described in previous

236 studies (Figs. 1C-G, ~~Fig.~~ 3A-E). Individual fibre diameters vary between 10-80 µm. Calcite fibres

237 terminate at individual concentric growth layers that also form the nucleation site for the overlying,

238 next fibre generation, displaying increasing thicknesses and occurring in increasing numbers towards

239 the outer portions of the rostrum (Fig. 1A-D). Brighter area in BSE are more likely to be composed of

240 near-stoichiometric $CaCO_3$ with higher average atomic masses (mainly Ca), whereas excess C, P, Mg,

241 or S will lower the average atomic mass. Accordingly, areas with decreasing amount of Ca and

242 increasing amounts of C, P, Mg or S are darker.

243 Four section planes are presented to describe the intricate bio-composite mineral present

244 within a single fibre. The following description distinguishes between the darker framework (i), i.e.,

245 micro~~n~~metre-thick branches terminating in wall-like reinforcements and (ii) tri-radial central

246 portions; and brighter fabric (iii) consisting of calcite crystals forming isopachous cement layers with

247 individual crystallites coated by submicro~~n~~metre thick layers of matter darker in BSE (Fig. 1G). In all

248 sections, we observed isopachous calcite crystals oriented perpendicular to the inner dark walls (Fig.

249 3A-E). Section plane I consists of three simple, dark in BSE branches of variable lengths. Often, these

250 branches exhibit reinforcements of variable lengths and thicknesses (about 1 micro~~n~~metre) and

251 increasing widths towards neighbo~~u~~ring branches (Figs. 1D-I, 3A). Conversely, reinforcements being

252 connected to neighboring triangles are rarely observed. Section type II is characterized by an

253 enlarged, dark in BSE central element of variable diameter (2-30 µm, Figs. 1D-II, 3C). Some of the

254 larger central elements display an inner zone with additional tri-radial structures comprising of

255 smaller, isopachous, brighter in BSE area calcite crystals rotated by 60° relative to outer branches

256 (Figs. 1D-III, 3D; section type III). Section type IV represents the most complex fabric. Here, the inner

257 portions of larger central elements display alternating darker and brighter in BSE areas (Figs. 1D-IV,

258 3E). Generally, enlarged central elements correlate with a shortening of corresponding, darker

259 branches.

260   Thin sections cut parallel to the c-axis of the radiaxial fibrous calcite reveal an framework dark in

261 BSE of triangular shaped elements with their tips pointing towards the outer margin of the rostrum

262 (Fig. 1C-D, supplement Fig. 2). Lighter and darker areas within a single calcite fibre show their

263 composite nature. Lighter and darker areas within concentric growth rings, as visible in transmitted

264 light, depend on the number and size of these elements. Higher magnification reveals a homogenous

265 central portion ("trunk" – white line) of pyramidal morphology dark in BSE surrounded by inclined

266 isopachous calcite crystals coated by material dark in BSE. This overall pattern results in a "~~x~~

267 Christmas tree like" structure (Fig. 3F). The dark framework forms the substratum upon which an

268 isopachous, translucent calcite phase nucleated (Fig. 1D, G 2-3). The boundary surface between the

269 framework dark in BSE and the surrounding carbonates brighter in BSE is, in places, corroded and

270 uneven (Fig. 2).

271

272 *3.3   Electron microprobe analysis (EMPA)*

273   The contrasting chemical composition of the two different calcite phases building these rostra is

274 also revealed by EMP data. Detailed WDS scans show that the strongest variability is displayed by

275 Mg, P, and S, whereas other elements are almost constant or ~~contained~~present in amounts close to

276 the detection limit (e.g., SrO = 0.1-0.2 wt.%; FeO = <0.1 wt.%; MnO < 0.5 wt.%. X-ray element

277 distribution ~~counts~~ maps show a generally low concentration of the elements Mg (MgO = 0.3-0.4

278 wt.%), P (P$_2$O$_5$ = 0.1-0.2 wt.%), and S (SO$_3$ = 0.20-0.50 wt.%). The Mg- and P-content is slightly

279 elevated in the darker, triangular areas in BSE images (MgO up to 0.6 wt.%; P$_2$O$_5$ up to 0.25 wt.%)

280 compared to the relatively brighter areas in BSE images in the centre of larger tetrahedrons and their

281 ~~surroundings~~vicinity. Lowest Mg ~~values~~ concentrations were ~~collected~~ found along microfractures

11

282 that ~~show a~~display bright luminescence ~~in CL~~colours (MgO < 0.2 wt.%; Fig. 6B). Sulfur has a higher

283 concentration in the brighter ~~in BSE~~ areas in BSE images (SO_3 up to 0.65 wt.%) and lower

284 concentrations in the darker areas in BSE ~~area~~images (~~(~~SO_3 = 0.20-0.50 wt.%; Fig. 6D). For better

285 comparison with BSE images from other samples and with the element distribution, ~~we collect~~ BSE

286 data were obtained for the same field of view (Fig. 6A).

287

288 *3.4 Electron Backscattered Diffraction imaging (EBSD)*

289 Electron backscattered diffraction was used to document the biological controlled (sensu

290 Lowenstam and Weiner, 1989; Dupraz et al., 2009; Weiner and Addadi, 2011) formation of what is

291 here assumed to represent the primary biogenic skeletal carbonate. EBSD reveals a very low

292 variation of c-axes orientation of calcite fibres (Fig. 4A). The sub-parallel orientation of the c-axes

293 {001} is documented by their close fitting in the lower hemisphere of a Schmidt net (Fig. 4E, left plot).

294 A different characteristic is found for the crystallographic orientation of the a-axes {010} of calcite

295 fibres (Fig. 4E, right plot). All a-axes are aligned along a great circle whilst the colour code of the

296 according fibres is indicative of an arrangement in bundles. Adjacent fibres (10 to 100 fibres) share a

297 similar - if not identical - orientation (Fig. 4A-B). The majority of fibre bundles are characterized by

298 blue, green and red colour coding. Specifically, the spatial orientation of individual a-axes within a

299 single fibre bundle deviates by 20° or less from the bundle mean value. Variation in the orientation of

300 the c-axis of a single calcite fibre in the range of 1-3° was observed (Fig. 4D). As the angular

301 resolution from blue to red rainbow colour shown in EBSD maps (Fig. 4A-B) has a resolution of 50°,

302 minor angular deviations (<1°) are not visible in ~~our image~~ Fig. 4A-B.

303

304 3.5 *Synchrotron radiation based micro-computed tomography (SRμCT)*

12

305   Tetrahedral structures are visible in three dimensions in the tomographic dataset despite the

306   high signal to noise ratio and artefacts. There is a distinct difference in X-ray attenuation between the

307   inner tri-radial elements and the surrounding calcite.

308

309   **4.   Interpretation and Discussion**

310   *4.1 Reconstruction of the primary belemnite rostrum ultrastructure*

311

312   Data presented here document a repeated pattern of triangular elements that seem to be

313   originally connected, building a concentric layered, highly complex, and porous framework. The

314   space between the former skeletal elements is interpreted as pore space probably filled by body

315   fluids or organic material during the life time of these organisms. The latter assumption is based on

316   analogous observations in the porous endoskeletons of recent *Sepia* (Sherrard, 2000; Guerra, 2006).

317   Referring to the high porosity observed in both, the belemnite rostraum and the sepiid cuttlebone, it

318   is important to note that these structures are not homologous (Fuchs 2012).

319   Accordingly, the belemnite rostra originally consisted of an organic-rich biogenic framework of

320   calcitic tri-radial tetrahedrons (triangular pyramids arranged perpendicular to the concentric layers

321   during lifetime). Tetrahedrons are elongated along their c-axis with the tip of the pyramid pointing

322   towards the precipitation site i.e., in growth direction towards the outer margin of the rostrum (Fig.

323   1C-D). Individual branches protruding from the edges of the tetrahedrons possess outer

324   reinforcements acting as stabilizers. The central portion of the tetrahedrons may yield a channel-like

325   cavity (Fig. 1D III-IV). Organic membranes at which nucleation of the tetrahedron may have started

326   and stopped are not preserved. However, it seems likely that such membranes were present because

327   the bases of the tetrahedrons follow a concentric layer. Structurally, the bundling of the tri-radial

328   elements forms a simple honeycomb-like framework in which the terminations of branches of

13

329 adjacent elements are connected. The mechanical stability of the honeycomb structure is enhanced

330 by reinforcement walls (Figs. 1D, G, 3C).

331 Based on the variable dimensions of skeletal elements seen in thin sections, intra-rostral pore

332 space was visually estimated to range between 50-90% of the total rostrum (Fig. 3A: 90% pore space

333 and 10% skeletal elements; Fig. 3B; 50% pore space and 50% skeletal elements). In this context, the

334 observation that pore space is not limited to the apical line region but is present across the bulk

335 rostrum is important. The secretion of a porous, but mechanically stable endoskeleton orthorostrum

336 is probably best seen in the context of a considerable reduction of energy and building material

337 required to form this structure compared to a massive structure endoskeleton (Sherrard, 2000).

338 Strict biological control, i.e. in the presence of organic templates (Chateigner et al., 2000; Richter et

339 al., 2011), over the precipitation of primary skeletal elements is demonstrated by a systematic

340 arrangement of adjacent elements into bundles of similar or identical orientation of their

341 crystallographic a-axes. This configuration results in a much higher mechanical load capacity and

342 torsion stiffness of the framework of the rostrum.

343 Alternating concentric Ca-rich (brighter; laminae obscurae) and C-rich layers (darker; laminae

344 pellucidae) of Müller-Stoll (1936) are related with the banded distribution of larger and smaller

345 organic-rich triangular elements of the primary skeletonal structure of the belemnite orthorostrum

346 (Fig. 1D, supplement Fig. 2). These layers potentially indicate differences in calcite precipitation rates.

347 Based on petrographic and ultrastructural evidence, the Mg and Ca elemental concentrations of the

348 rostrum, the lack of secondary micro-dolomite, and the absence of blotchy luminescence, the widely

349 held assumption of a primary low-Mg calcite mineralogy for the studied belemnite rostra is

350 confirmed (see discussion in Richter et al., 2003).

351

352 *4.2 Early and late diagenetic processes*

353

14

354   The presence of a highly porous primary rostrum architecture during the life time of the

355   belemnite organism as proposed here, is in contrasted byto the dense fabrics observed in the case of

356   most rostra collected in Mesozoic sedimentary successions (Fig. 1A-B). Hence, the diagenetic

357   pathway from porous to dense fabrics deserves attention. The marine diagenetic alteration of

358   biominerals is initiated directly after the death of a carbonate-secreting marine organism when

359   metabolic processes come to a halt. At this early stage, organic matter outside of the orthorostrum

360   (i.e., the belemnite animal itself) and in the pore space of rostra and between biominerals

361   decomposes (Saelen, 1989), triggering a series of complex bio-chemical processes. Essentially,

362   decomposition of organic matter is mediated by microbial activity, and given the abundance of

363   marine microbial life, there is no reason to assume that this would have been different in the case

364   examples studied here.

365   Microbial metabolic products, the presence of microbial "mucus" (extracellular polymeric

366   substance) and charged surfaces represented by microbial bodies influence the micro-environment

367   in intra-rostrum pore space by altering the balance between more reduced and more oxidized forms

368   of carbon as previously summarized under the term "alkalinity engine" (Dupraz et al., 2009).

369   Specifically, Visscher and Stolz (2005) subdivided microbial species into 5-7 groups ("guilds") having a

370   similar metabolism. Some of these promote carbonate precipitation (e.g., cyanobacteria, sulphate

371   reducers), whilst others favour dissolution (e.g., aerobic heterotrophs, fermenters). Dupraz et al.

372   (2009) documented that the balance of microbial metabolic activities directly influences carbonate

373   precipitation or, vice versa, dissolution. Initial microbial decomposition of organic matter may result

374   in the production of organic acids lowering the pH-values in the pore space (Berner et al., 1978),

375   enhancing intra-skeleton orthorostrum dissolution of biominerals (Fig. 2).

376   As soon as the bulk of organic matter is decomposed, alkalinity is increased due to microbial

377   metabolic   products   enhancing   the   precipitation   of   carbonate   minerals   (intrinsic

378   organomineralization) leading – in the view of the authors - to the formation of the translucent,

379   isopachous calcite crystals that occlude primary pore space in rostra (Fig. 2). Obviously, any

380 assumption regarding microbial processes in these ancient carbonates must remain speculative.

381 Nevertheless, following the basic concepts laid out in Dupraz et al. (2009), we tentatively assume

382 that a first phase of decomposition was dominated by aerobic heterotrophy, sulphide oxidation, and

383 fermentation decreasing the saturation index and resulting in the corrosion of skeletal elements in

384 the belemnite rostrum. Evidence for this comes from micro-corrosion features at the outer surfaces

385 of the primary skeletal framework forming the substratum upon which the pore-filling, secondary

386 calcite phase nucleates (Fig. 2).

387   The nucleation and precipitation of the secondary calcite phase (Fig. 1D, G, 2-3) was possibly

388 dominated by sulphate reduction increasing the saturation index and hence favoring precipitation of

389 $CaCO_3$. During crystals growth, remnants of belemnite organic matter combined with microbial

390 mucus were likely trapped between single crystals or at the growth front of crystals and delineate

391 crystal boundaries. Specifically, the growth of fibrous calcitic crystals will proceed as long as growth

392 rate, fluid supersaturation, and temperature are low enough to discourage spontaneous nucleation

393 (Oti et al., 1989). Similar processes have been described from extant echinoderm ~~endoskeletons~~

394 ~~skeletal remains~~that share a comparable amount of primary porosity ~~like the herein~~with the

395 described belemnite orthorostra (Richter et al., 2003).

396   During this early stage of diagenetic evolution, the rostra most likely preserved their original

397 morphology due to the biogenic calcite framework and abiogenic calcite progressively occluding

398 former pore space preventing, in combination, a collapse of the ~~endoskeletons~~rostra. The directly

399 comparable, dark blue intrinsic luminescence of the translucent secondary outer calcite layer and the

400 calcite infill of central pore space of many of the larger triangles (Figs. 3D-E, 5A, D, 6) suggest that

401 both phases precipitated from one fluid, or different fluids with near-identical geochemistry. This is,

402 of course, within the limitations of the geochemical resolution of the ~~CL~~ cathodoluminescence

403 method and with reference to elements that affect luminescence patterns (e.g., Mn^{2+}, Fe^{2+} and REE;

404 see discussion in Barbin 1991, 1993; Ritter et al., 2015). Conversely, the organic matter-rich triangles

405 display a moderately brighter blue luminescence pattern (Fig. 5C, F). This feature is best explained by

406 calcite lattice deformation due to the incorporation of organic matter into the crystal lattice

407 (intracrystalline) and is not necessarily indicative of a different geochemical composition. This

408 concept is supported by x-ray diffractometry (Richter et al., 2011) documenting that the fibrous

409 fabric of the belemnite rostra, lacking late diagenetic Mn-rich cements, is composed of

410 stoichiometric or near-stoichiometric calcites (d (104) = 3.030 to 3.035 Å).

411   A late diagenetic (burial) stage of rostra is documented by dissolution and compaction features

412 as indicated by microfractures and microstylolites (Figs. 2, 5C, F; Rosales et al., 2004a, b). The

413 circulation of Mn^{2+}-rich fluids caused the precipitation of a late calcite phase that occludes fractures

414 and fissures. In some cases this late phase yields a bright luminescence and is zigzag or triangular

415 shaped, tracing the morphology of the triangular biominerals (Fig. 5C).

416

417 *4.3 Implications for the function of the rostrum*

418

419   It is generally accepted that the belemnite rostrum acts as a counterweight to the soft body.

420 Based on the observation of a high primary porosity (see also Spaeth, 1971, 1973, 1975; Ullmann et

421 al., 2015), this interpretation requires renewed consideration. Rostra are commonly considered to

422 have the same density as inorganic calcite crystals, ranging from 2.5-2.7 g/cm³.

423   *Sepia*, the closest living relative of the extinct belemnites, incorporates a total of 10-40% organic

424 matter in its cuttlebone shell and comparably high amounts of intracrystalline organics were

425 observed for the biogenic belemnite skeletonorthorostrum. Accordingly, ignoring open pore space, a

426 reduced density of the biogenic belemnite calcite of about 2.4 g/cm³ (10% organic) – 2.0 g/cm³ (40%

427 organic) results. Assuming that liquid or extracrystalline organic matter (1.03 g/cm³) - with density

428 comparable to that of seawater (1.026 g/cm³) - filled up the pore space of living belemnite rostra, an

429 overall density of the rostrum ranging between roughly 1.7-1.1 g/cm³ (mean 1.4 g/cm³) is tentatively

430 assumed on the level of a working hypothesis. If these assumptions hold true, then the belemnite

431   rostrum had a cumulative density that is significantly lower than that of stoichiometric calcite.

432   Therefore, questions regarding the locomotion of belemnites result.

433   A possible analogue may come from a structure reported from a modern

434   onychoteut~~mmastrep~~hid squid (*Onykia*) that has remarkable morphological similarity to the

435   *Megateuthis* rostrum. *Onykia* has a purely organic rostrum that due to its very low density does not

436   act as a counterweight for the soft body. It is assumed that it supports the posterior part of the

437   mantle and fins (= axial stability in Bizikov and Arkhipkin, 1997 and Arkhipin et al., 2015). A function

438   as a muscle attachment structure for belemnite rostra ~~h~~was ~~been~~ first put forward by Stevens

439   (1965). Direct evidence for the presence of fins in belemnites has recently reported by Klug et al.

440   (2015), favouring a squid-like high speed swimming ~~in~~mode of life for Jurassic belemnites.

441   Noteworthy to report here, is the case of belemnites (*Chitinoteuthis*) with a non-calcified rostrum

442   (Müller-Stoll, 1936).

443

444   **5 Open questions and suggestions for future research**

445   5.1. Paragenesis of porosity-occluding calcite phase

446   Within individual belemnite rostra, data presented here differentiate: (i) a~~the~~ biogenic, highly

447   porous skeletal framework secreted during the life time of the ~~belemnite~~organism; (ii) ~~the~~ an

448   inorganic or organomineralic – arguably early diagenetic - calcite phase occluding the pore space of

449   the biogenic framework; and (iii) a late diagenetic, burial, Mn-rich carbonate phase filling fissures and

450   larger cracks within the rostra. Assuming that the above-discussed paragenetic succession is valid, a

451   series of open questions result~~.~~: In the view of the authors, it is at least conceivable that portions of

452   the rostral pore space were occluded during the life time of the belemnites (remote

453   biomineralization sensu Hücker and Hemleben, 1976; Chinzei and Seilacher, 1993; Seilacher and

454   Chinzei, 1993). If this holds true, then the paragenetic sequence of primary framework and

455   secondary infill calcite is even more complicated than presented here and gradual in nature.

456   Moreover, individual growth increments within rostra are then not representative of specific

457 correlative time intervals. Specifically, each growth increment then represents a complex composite

458 structure of paragenetic phases representing temporally different stages in the belemnite

459 ontogenetic cycle. Obviously, this would render the interpretation of time series belemnite

460 geochemical data difficult. Evidence against a biogenic infill of the skeletal pore space by remote

461 biomineralization sensu Seilacher and Chinzei (1993), however, may or may not come from the

462 presence of a corroded outer surface of what is considered the primary skeletal ultrastructure of

463 these rostra (Fig. 2). It seems difficult to argue that intra-rostrum body fluids became corrosive at

464 some stage during the life time of the belemnite animal. Clearly, these questions require further

465 detailed work.

466

467 *5.2 Primary skeletal ultrastructure and preservation of organic matter*

468

469   The authors acknowledge the fact that despite the very detailed information regarding the

470 belemnite ultrastructure shown here, our study lacks direct evidence for a primary biogenic origin of

471 the complex, highly porous framework and the subsequent cementation by an early diagenetic

472 calcite phase. Open questions, however, remain. Specifically, the significance of preserved organic

473 matter in the biogenic belemnite calcite deserves attention. In the following, we present several lines

474 (petrographic, optical, and geochemical data) of circumstantial evidence suggesting the presence of

475 preserved organic matter.

476   The sector-wise systematic arrangement of triangular elements - with their a-axis being

477 oriented subparallel to parallel (Figs. 3A-C, 4A-B, 5A, D) - in bundles, indicate a biologically controlled

478 origin (Lowenstam and Weiner, 1989) of these fabrics. The primary belemnite rostrum ultrastructure

479 is brownish (Figs. 5A, 7A) in thin sections under transmitted light and has a relatively low optical

480 relief. According to Ullmann et al. (2014), brownish areas in thin sections of biogenic carbonates are

481 indicative of remnant organic matter (C_{org}). Under the cathodoluminescence- and fluorescence

482 microscope, the primary filigree belemnite framework shows a light blue luminescence (CL) and light

19

483 green fluorescence (FL). According to Wanamaker et al. (2009) and Pérez-Huerta et al. (2008),

484 fluorescence in biominerals is triggered by organic macromolecules associated with chitin

485 polysaccharides and proteins. Dark fluorescence patterns commonly refer to portions of the skeletal

486 hardparts that are relatively depleted in organic matter. Bright green fluorescence patterns typify

487 areas with increased amount of organic matter (Wanamaker et al., 2009).

488 Primary skeletal structures display darker colours in SEM-BSE images. Electron microprobe

489 analyses revealed that the biogenic skeletal calcites contain more P and Mg but less S compared to

490 what is here considered an early diagenetic, pore-filling calcite phase. Higher concentrations of P (Fig.

491 6C) may be related to the presence of organic matter. Arguments for this have been presented by

492 Longinelli et al. (2002, 2003) and Gröcke et al. (2003) who found phosphate (PO_4^{3-}) of presumed

493 biogenic origin being preferentially enriched along concentric growth rings. Generally, the phosphate

494 concentration of ancient belemnite rostra is variable but very low (less than 0.3%) comparable to

495 that in ~~Recent~~ modern *Sepia*.

496 The primary filigree belemnite framework does not fluoresce under the CLFM. The factors

497 that cause fluorescence in samples studied under the CLFM are poorly constrained (Fig. 8). Naturally-

498 occurring organic compounds such as proteins or polysaccharides can cause fluorescence in other

499 biogenic carbonates, including brachiopods (Pérez-Huerta et al., 2008), gastropods (Guzman et al.,

500 2007), or cephalopods (Linzmeier et al., 2016). In modern brachiopods and *Nautilus*, portions of the

501 exoskeletons with higher amounts of intracrystalline organic matter (Clark, 1999) appear dark under

502 CLFM (~~-~~Pérez-Huerta et al., 2008; Linzmeier et al., 2016~~; Pérez-Huerta et al., 2008~~). This pattern lends

503 support to the argument that dark triangular areas in BSE images represent the primary biogenic

504 skeleton and contain remnants of organic matter. Marine sediments may contain abundant humic

505 substances resulting from the degradation of marine organic matter (Nissenbaum and Kaplan, 1972)

506 and evidence has been presented that the sul~~f~~phur content of the humic substances increases with

507 degradation (Francois 1987). Concluding, it is here proposed that humic substances caused elevated

508 S concentrations in the diagenetic calcite phase that occludes the skeletal pore space (Fig. 6D) and

20

509 causes the CLFM fluorescence in all three wavelengths (Blyth et al., 2008; Orland et al., 2009, 2012;

510 Fig. 8).

511   Similarly, microtomographic data indicate the former presence of organic matter in dark

512 triangular areas of rostra (Fig. 9) as observed in BSE images. The brightness of a carbonate observed

513 in CT image indicates the degree of attenuation of an X-ray passing through this material (Mobilio et

514 al., 2015). As the inner tri-radial structures of rostra appear darker in colour relative to the calcite

515 phase fringing these structures, we suggest that the fringing phase is made of a denser calcite phase

516 compared to the inner structure. That observation is in line with the observation of a low optical

517 relief of these features (supplement Fig. 1A-B).

518   This ~~tentative~~ interpretation presented here with regard to belemnite rostra is arguably

519 consistent with observations of 10-40% organic matrix in the *Sepia* cuttlebone (Birchall and Thomas,

520 1983; Florek et al., 2009). This is relevant as we suggest that the belemnite rostrum is structurally

521 similar but not homologous (Fuchs 2012) to the *Sepia* cuttlebone with regard to the primary intra-

522 skeletal porosity. Having said this, the presence of preserved organic matter in ancient biogenic

523 carbonates particularly, intra-crystalline organic matter is not uncommon (Clark, 1999, 2005). Excess

524 carbon observed for *Megateuthis* has been interpreted as evidence for a former organic matrix

525 within these low-Mg calcite biominerals (Dunca et al., 2006). Similarly, Florek (2004) argued for an

526 excess of carbon in the rostra of *Belemnopsis* and *Hibolites*. Summing up: Different lines of

527 circumstantial evidence point to the presence of remnant organic matter within biominerals. These

528 data require verification or rejection via the application of spatially highly resolved geochemical data.

529 This work is presently ~~under~~ in progress.

530

531 **5. Conclusions**

532   Ultrastructural data documented here suggest that the calcitic rostra of Mesozoic belemnites

533 yielded 50-90% primary porosity probably filled with body fluids and/or organic matter during the life

534 time of the animal. Porosity was distributed throughout the rostrum as opposed to being limited to

Formatted: No underline, Font color: Auto

535   the central apical area. The primary biogenic rostrum framework consists of triaxial branches and

536   tetrahedrons of variable size forming a honeycomb-like network. This structure arguably combined

537   mechanical stability with an energy-efficient biomineralization strategy.

538   The recognition of belemnite rostra as a highly porous structure requires a re-interpretation of

539   the function of the rostrum as counterweight to the soft body and has implications for the swimming

540   mode of belemnites. On the level of a working hypothesis, we argue that the low-porosity fabric

541   found in fossil rostra collected in outcrops worldwide is the result of a syntaxial, early diagenetic

542   cement phase that nucleated upon the surface of the biogenic framework and subsequently

543   occluded the pore space. The possibility of gradual occlusion of skeletal porosity by remote

544   biomineralization during later ontogenetic stages during the life of the animal is possible but seems

545   unlikely at present.

546   If the here-presented concepts hold true, then these new findings have significant implications

547   with regard to geochemical proxy data collected from fossil belemnite rostra. Specifically, the fact

548   that rostra may consist of biogenic and abiogenic calcite phases formed at different times may

549   explain the controversially low reconstructed seawater temperatures and the uncommonly high

550   scatter of proxy data even from well-preserved rostra collected in the same stratigraphic interval.

551   This is because seawater properties of surficial water masses, the habitat of nektobenthic

552   belemnites, are recorded in the biogenic portions of the rostrum whereas the early diagenetic phase

553   reflects cooler basinal bottom or marine pore water signatures. Findings presented here form a solid

554   and well-constrained petrographic data set but one that must be verified by high-resolution

555   geochemical data of all paragenetic calcite phases observed.

556

557

558   **6. Acknowledgement**

22

561 making this study possible (H. Schwandt, P. Girod, G. Grimmberger, J. Kalbe, M. Sowiak and others).

562 We acknowledge the comments by the two journal reviewers I. Jarvis and D. Fuchs and the editorial

563 handling by Brian Jones. s improving an earlier version of that manuscript

564

7. References

566 Anderson, T.F., Popp, B.N., Williams, A.C., Ho, L.Z., Hudson, J.D., 1994. The stable isotopic records of

567 fossils from the Peterborough Member, Oxford Clay Formation (Jurassic), UK:

568 palaeoenvironmental implications. Journal of the Geological Society, London 151, 125-138.

569 Arkhipkin, A., Weis, R., Mariotti, N., Shcherbich, Z., 2015. "Tailed" Cephalopods. Journal of Molluscan

570 Studies 81, 345-355.

571 Barbin, V., 1991. Fluctuation in shell composition in *Nautilus* (Cephalopoda, Mollusca): evidence from

572 Cathodoluminescence. Lethaia 25, 391-400.

573 Barbin, V., 2013. Application of cathodoluminescence microscopy to recent and past biological

574 materials: a decade of progress. Mineralogy and Petrology 107, 353-362.

575 Benito, M.I., Reolid, M., 2012. Belemnite taphonomy (Upper Jurassic, Western Tethys) part II: Fossil-

576 diagenetic analysis including combined petrographic and geochemical techniques.

577 Palaeogeography, Palaeoclimatology, Palaeoecology 358, 89-108.

578 Berner, R.A., Westrich, J.T., Graber, R., Smith, J., Martens, C.S., 1978. Inhibition of aragonite

579 precipitation from supersaturated seawater: a laboratory and field study. American Journal of

580 Science 278, 816-837.

581 Birchall, J.D., Thomas, N.L., 1983. On the architecture and function of cuttlefish bone. Journal of

582 Materials Science 18, 2081-2086.

583 Bizikov, V.A., Arkhipkin, A.I., 1997. Morphology and microstructure of the gladius and statolith from

584 the boreal Pacific giant squid *Moroteuthis robusta* (Oegopsida; Onychoteuthidae). Journal of

585 Zoology 241, 475-492.

586 Blyth, A.J., Baker, A., Collins, M.J., Penkman, K.E.H., Gilmour, M.A., Moss, J.S., 2008. Molecular

587 organic matter in speleothems and its potential as an environmental proxy. Quaternary Science

588 Reviews 27, 905–921.

589 Chateigner, D., Hedegaard, C., Wenk, H.R., 2000. Mollusc shell microstructures and crystallographic

590 textures. Journal of Structural Geology 22, 1723-1735.

591 Chinzei, K., Seilacher, A., 1993. Remote Biomineralization I: Fill skeletons in vesicular oyster shells.

592 Neues Jahrbuch für Geologie und Paläontologie, Abhandlungen 190, 349-361.

593 Clark, II G.R., 1999. Organic matrix taphonomy in some molluscan shell microstructures.

594 Palaeogeography, Palaeoclimatology, Palaeoecology 149, 305-312.

595 Clark, II G.R., 2005. Organic matrix in the porifera and Cnidaria: déjà vu through a temporal

596 telescope. Geological society of America Abstracts with Program 37, 366.

597 Cochran, J.K., Landman, N.H., Turekian, K.K., Michard, A., Schrag, D.P., 2003. Paleoceanography of

598 the Late Cretaceous (Maastrichtian) Western Interior Seaway of North America: evidence from Sr

599 and O isotopes. Palaeogeography Palaeoclimatology Palaeoecology 191, 45-64.

600 Cochran, J.K., Kallenberg, K., Landman, N.H., Weinreb, D., Turekian, K.K., Beck, A.J., Cobban, W.A.,

601 2010. Effect of diagenesis on the Sr, O, and C isotope composition of Late Cretaceous Mollusks

602 from the Western Interior Seaway of North America. American Journal of Science 310, 69-88.

603 Coronado, I., Pérez-Huerta, A., Rodríguez, S., 2013. Primary biogenic skeletal structures in

604 Multithecopora (Tabulata, Pennsylvanian). Palaeogeography, Palaeoclimatology, Palaeoecology

605 386, 286-299.

606 Dunca, E., Doguzhaeva, L., Schöne, B.R., Schootbrugge, B. v.d., 2006. Growth patterns in rostra of the

607 Middle Jurassic belemnite *Megateuthis giganteus*: controlled by the moon? Acta Universitatis

608 Carolinae – Geologica 49, 107-117.

609 Dupraz, C., Reid, R.P., Braissant, O., Decho, A.W., Norman, R.S., Visscher, P.T., 2009. Processes of

610 carbonate precipitation in modern microbial mats. Earth-Science Reviews 96, 141-162.

611   Dutton, A., Huber, B.T., Lohmann, K.C., Zinsmeister, W.J., 2007. High-Resolution Stable Isotope

612   Profiles of a Dimitobelid Belemnite: Implications for Paleodepth Habitat and Late Maastrichtian

613   Climate Seasonality. Palaios 22, 642–650.

614   Florek, M., Youn, H.S., Ro, C.U., Wierzbowski, H., Osán, J., Kazimierczak, W., Kuczumow, A., 2004.

615   Investigation of chemical composition of belemnite rostra by synchrotron-based X-ray

616   microfluorescence and diffraction and electron microprobe. Journal of Alloys and Compounds

617   362, 99-106.

618   Florek, M., Fornal, E., Gomez-Romero, P., Zieba, E., Paszkowicz, W., Lekki, J., Nowak, J., Kuczumow,

619   A., 2009. Complementary microstructural and chemical analyses of *Sepia officinalis*

620   endoskeleton. Materials Science and Engineering C 29, 1220-1226.

621   Francois, R., 1987. A study of sulphur enrichment in the humic fraction of marine sediments during

622   early diagenesis. Geochimica et Cosmochimica Acta 51, 17–27.

623   Fuchs, D., 2012. The "rostrum"-problem in coleoid terminology – an attempt to clarify

624   inconsistencies. Geobios 45, 29-39.

625   Goetz, A.J., Steinmetz, D.R., Griesshaber, E., Zaefferer, S., Raabe, D., Kelm, K., Irsen, S., Sehrbrock, A.,

626   Schmahl, W.W., 2011. Interdigitating biocalcite dendrites from a 3-D jigsaw structure in

627   brachiopod shells. Acta Biomaterialia 7, 2237-2243.

628   Gröcke, D.R., Price, G.D., Ruffell, A.H., Mutterlose, J., Baraboschkin, E., 2003. Isotopic evidence for

629   Late Jurassic-Early Cretaceous climate change. Palaeogeography, Palaeoclimatology,

630   Palaeoecology 202, 97-118.

631   Guerra, A., 2006. Ecology of *Sepia officinalis*. Vie et Milieu – Life & Environment 56, 97-107.

632   Guzman, N., Ball, A.D., Cuif, J.-P., Dauphin, Y., Denis, A., Ortlieb, L., 2007. Subdaily growth patterns

633   and organo-mineral nanostructure of the growth layers in the calcitic prisms of the shell of

634   *Concholepas concholepas* Bruguière, 1789 (Gastropoda, Muricidae). Microscopy and

635   Microanalysis 13, 397-403.

636 Huber, B.T., Hodell, D.A., 1996. Middle-Late Cretaceous climate of the Southern high latitudes: Stable

637   isotopic evidence for minimal equator-to-pole thermal gradients: Discussion and reply.

638   Geological Society of America Bulletin 108, 1193-1196.

639 Hückel, U., Hemleben, C., 1976. Diagenetische Spurenelement-Verschiebungen und Veränderungen

640   der Skelett-Strukturen bei Belemniten Rostren. Zentralblatt Geologie und Paläontologie Teil II

641   1976, 362-365.

642 Immenhauser, A., Schöne, B.R., Hoffmann, R., Niedermayr, A., 2016. Mollusc and brachiopod skeletal

643   hard parts: Intricate archives of their marine environment. Sedimentology 63, 1-59.

644 Jarvis, I., Trabucho-Alexandre, J., Gröcke, D., Uličný, D., Laurin, J., 2015. Intercontinental correlation

645   of organic carbon and carbonate stable isotope records: evidence of climate and sea-level change

646   during the Turonian (Cretaceous). The Depositional Record 1, 53-90.

647 Klug, C., Schweigert, G., Fuchs, D., Kruta, I., Tischlinger, H., 2015. Adaptations to squid-style high-

648   speed swimming in Jurassic belemnitids. Biological Letters 12, 1-5.

649 Kozdon, R., Kelly, D.C., Kita, N.T., Fournelle, J.H., Valley, J.W., 2011. Planktonic foraminiferal oxygen

650   isotope analysis by ion microprobe technique suggests warm tropical sea surface temperatures

651   during the Early Paleogene. Paleoceanography 26, 1-17.

652 Li, Q., 2011. Belemnite Palaeo-proxies and Dating of Mesozoic Carbonates. Ph.D. Thesis. 1-262,

653   Department of Earth Sciences, Univeristy College London.

654 Li, Q., McArthur, J.M., Atkinson, T.C., 2012. Lower Jurassic belemnites as indicators of palaeo-

655   temperature. Palaeogeography Palaeoclimatology, Palaeoecology 315, 38-45.

656 Li, Q., McArthur, J.M., Doyle, P., Janssen, N., Leng, M.J., Müller, W., Reboulet, S., 2013. Evaluating

657   Mg/Ca in belemnite calcite as a palaeo-proxy. Palaeogeography Palaeoclimatology,

658   Palaeoecology 388, 98-108.

659 Linzmeier, B.J., Kozdon, R., Peters, S.E., Valley, J.W., 2016. Oxygen isotope variability within *Nautilus*

660   shell growth bands. PLoS ONE (Accepted).

Formatted: Font: 11 pt, No underline, English (United Kingdom)

661   Longinelli, A., Iacumin, P., Ramigni, M., 2002. δ^{18}O of carbonate, quartz and phosphate from

662   belemnite guards: implications for the isotopic record of old fossils and the isotopic composition

663   of ancient seawater. Earth and Planetary Science Letters 203, 445-459.

664   Longinelli, A., Wierzbowski, H., Matteo, A. di, 2003. δ^{18}O(PO_4^{3-}) and δ^{18}O($CO32-$) from belemnite

665   guards from Eastern Europe: implications for palaeoceanographic reconstructions and for the

666   preservation of pristine isotopic values. Earth and Planetary Science Letters 209, 337-350.

667   Lowenstam, H.A., Weiner, S., 1989. On Biomineralization. Oxford University Press, New York 324 pp.

668   Lukeneder, A., Harzhauser, M., Müllegger, S., Piller, W.E., 2010. Ontogeny and habitat change in

669   Mesozoic cephalopods revealed by stable isotopes (δ^{18}O, δ^{13}C). Earth and Planetary Science

670   Letters 296, 103-114.

671   Massonne, H.-J., Neuser, R.D., 2005. Ilmenite exsolution in olivine from the serpentinite body at

672   Zöblitz, Saxonian Erzgebirge – microstructural evidence using EBSD. Mineralogical Magazine 69,

673   119-124.

674   McArthur, J.M., Janssen, N.M.M., Reboulet, S., Leng, M.J., Thirlwall, M.F., Schootbrugge, B. v.d.,

675   2007. Palaeotemperatures, polar ice-volume, and isotope stratigraphy (Mg/Ca, δ^{18}O, δ^{13}C,

676   ^{87}Sr/^{86}Sr): The Early Cretaceous (Berriasian, Valanginian, Hauterivian). Palaeogeography

677   Palaeoclimatology, Palaeoecology 248, 391-430.

678   Mobilio, S., Boscherini, F., Meneghini, C., 2015. Synchrotron Radiation: Basics, Methods and

679   Applications. Springer Berlin Heidelberg.

680   Mokso, R., Marone, F., Irvine, S., Nyvlt, M., Schwyn, D., Mader, K., Taylor, G.K., Krapp, H.G., Skeren,

681   M., Stampanoni, M., 2013. Advantages of phase retrieval for fast X-ray tomographic microscopy.

682   Journal of Physics D: Applied Physics 46, 1-12.

683   Müller-Stoll, H., 1936. Beiträge zur Anatomie der Belemnoidea. Nova Acta Leopoldina-Abhandlungen

684   der Kaiserlich Leopoldinisch-Carolinisch Deutschen Akademie der Naturforscher, Neue Folge 4, 1-

685   70.

686 Neuser, R.D., Bruhn, F., Götze, J., Habermann, D., Richter, D.K., 1996. Kathodolumineszenz: Methodik

687 und Anwendung. Zentralblatt Geologie und Paläontologie Teil 1 1995, 287-306.

688 Niebuhr, B., 1995. Fazies-Differenzierungen und ihre Steuerungsfaktoren in der höheren Oberkreide

689 von S-Niedersachsen/Sachsen-Anhalt (N-Deutschland). Berliner Geowissenschaftliche

690 Abhandlungen, Reihe A 174, 1-131.

691 Niebuhr, B., Hiss, M., Kaplan, U., Tröger, K.A., Voigt, S., Voigt, T., Wiese, F., Wilmsen, M., 2007.

692 Lithostratigraphie der norddeutschen Oberkreide. Schriftenreihe der Deutschen Gesellschaft für

693 Geowissenschaften 55, 1-136.

694 Nissenbaum, A., Kaplan, I.R., 1972. Chemical and isotopic evidence for the *in situ* origin of marine

695 humic substances. Limnology and Oceanography 17, 570-582.

696 Orland, I.J., Bar-Matthews, M., Kita, N.T., Ayalon, A., Matthews, A., & Valley, J.W., 2009. Climate

697 deterioration in the Eastern Mediterranean as revealed by ion microprobe analysis of a

698 speleothem that grew from 2.2 to 0.9 ka in Soreq Cave, Israel. Quaternary Research 71, 27–35.

699 Orland, I.J., Bar-Matthews, M., Ayalon, A., Matthews, A., Kozdon, R., Ushikubo, T., Valley, J.W., 2012.

700 Seasonal resolution of Eastern Mediterranean climate change since 34 ka from a Soreq Cave

701 speleothem. Geochimica et Cosmochimica Acta 89, 240–255.

702 Oti, M.N., Ogbuji, L.U., Breuer, K.H., 1989. Diagenetic transformation of magnesium calcite in a

703 monocrystalline rock-forming carbonate skeleton of an echinoderm. Chemical Geology 76, 303-

704 308.

705 Parkinson, D., Curry, G.B., Cusack, M., Fallick, A.E., 2005. Shell structure, patterns and trends of

706 oxygen and carbon stable isotopes in modern brachiopod shells. Chemical Geology 219, 193-235.

707 Podlaha, O.G., Mutterlose, J., Veizer, J., 1998. Preservation of $\delta^{18}O$ and $\delta^{13}C$ in belemnite rostra from

708 the Jurassic/Early Cretaceous successions. American Journal of Science 298, 324-347.

709 Price, G.D., Page, K.N., 2008. A carbon and oxygen isotopic analysis of molluscan faunas from the

710 Callovian-Oxfordian boundary at Redcliff Point, Weymouth, Dorset: implications for belemnite

711 behaviour. Proceedings of the Geologists´ Association 119, 153-160.

712   Price, G.D., Sellwood, B.W., 1997. "Warm" palaeotemperatures fron high Late Jurassic

713   palaeolatitudes (Falkland Plateau): Ecological, environmental or diagenetic controls?

714   Palaeogeography Palaeoclimatology, Palaeoecology 129, 315-327.

715   Price, G.D., Wilkinson, D., Hart, M.B., Page, K.N., Grimes, S.T., 2009. Isotopic analysis of coexisting

716   Late Jurassic fish otoliths and molluscs: Implications for upper-ocean water temperature

717   estimates. Geology 37, 215-218.

718   Price, G.D., Fözy, I., Janssen, N.M.M., Pálfy, J., 2011. Late Valanginian-Barremian (Early Cretaceous)

719   palaeotemperatures inferred from belemnite stable isotope and Mg/Ca ratios from Bersek

720   Quarry (Gerecse Mountains, Trandanubian Range, Hungary). Palaeogeography

721   Palaeoclimatology, Palaeoecology 305, 1-9.

722   Price, G.D., Hart, M.B., Wilby, P.R., Page, K.N., 2015. Isotopic analysis of Jurassic (Callovian) molluscs

723   from the Christian Malford Lagerstätte (UK): Implications for ocean water temperature estimates

724   based on belemnoids. Palaios 30, 645-654.

725   Richter, D.K., Götte, T., Götze, J., Neuser, R.D., 2003. Progress in application of cathodoluminescence

726   (CL) in sedimentary petrology. Mineralogy and Petrology 79, 127-166.

727   Richter, D.K., Neuser, R.D., Schreuer, J., Gies, H., Immenhauser, A., 2011. Radiaxial-fibrous calcites: a

728   new look on an old problem. Sedimentary Geology 239, 23-36.

729   Ritter, A.-C., Kluge, T., Berndt, J., Richter, D.K., John, C.M., Bodin, S., Immenhauser, A., 2015.

730   Application of redox sensitive proxies and carbonate clumped isotopes to Mesozoic and

731   Palaeozoic radiaxial fibrous cements. Chemical Geology 417, 306-321.

732   Ritter, A.-C., Mavromatis, V., Dietzel, M., Wiethoff, F., Griesshaber, E., Casella, L., Schmahl, W.,

733   Koelen, J., Neuser, R.D., Leis, A., Buhl, D., Niedermayr, A., Bernasconi, S.M., Immenhauser, A.

734   (submitted). Experimental diagenesis: I – Exploring the impact of diagenesis on (isotope)

735   geochemical and microstructural features in biogenic aragonite. Geochimica et Cosmochimica

736   Acta.

737 Rosales, I., Quesada, S., Robles, S., 2001. Primary and diagenetic isotopic signals in fossils and

738 hemipelagic carbonates: the Lower Jurassic of northern Spain. Sedimentology 48, 1149-1169.

739 Rosales, I., Quesada, S., Robles, S., 2004a. Paleotemperature variations of Early Jurassic seawater

740 recorded in geochemical trends of belemnites from the Basque-Cantabrian basin, northern Spain.

741 Palaeogeography, Palaeoclimatology, Palaeoecology 203, 253-275.

742 Rosales, I., Robles, S., Quesada, S., 2004b. Elemental and oxygen isotope composition of Early

743 Jurassic Belemnites: Salinity vs. Temperature signals. Journal of Sedimentary Research 74, 342-

744 354.

745 Saelen, G., 1989. Diagenesis and construction of the belemnite rostrum. Palaeontology 32, 765-798.

746 Seilacher, A., Chinzei, K., 1993. Remote Biomineralization 2: Fill skeletons controlling buoyancy in

747 shelled cephalopods. Neues Jahrbuch für Geologie und Paläontologie, Abhandlungen 190, 363-

748 373.

749 Sessa, J.A., Larina, E., Knoll, K., Garb, M., Cochran, J.K., Huber, B.T., MacLeod, K.G., Landman, N.H.,

750 2015. Ammonite habitat revealed via isotopic composition and comparisons with co-occurring

751 benthic and planktonic organisms. Proceedings of the National Academy of Sciences of the

752 United States of America 112, 15562-15567.

753 Sherrard, K.M., 2000. Cuttlebone Morphology Limits Habitat Depth in Eleven Species of *Sepia*

754 (Cephalopoda: Sepiidae). Biological Bulletin 198, 404-414.

755 Spaeth, C., 1971. Aragonitische und calcitische Primärstrukturen im Schalenbau eines Belemniten aus

756 der englischen Unterkreide. Paläontologische Zeitschrift 45, 33-40.

757 Spaeth, C., 1973. Weitere Untersuchungen der Primär- und Fremdstrukturen in calcitischen und

758 aragonitischen Schalenlagen englischer Unterkreide-Belemniten. Paläontologische Zeitschrift 47,

759 163-174

760 Spaeth, C., 1975. Zur Frage der Schwimmverhältnisse bei Belemniten in Abhängigkeit vom

761 Primärgefüge der Hartteile. Paläontologische Zeitschrift 49, 321-331.

762   Stevens, G.R., 1965. The Jurassic and Cretaceous Belemnites of New Zealand and a Review of the

763   Jurassic and Cretaceous Belemnites of the Indo-Pacific Region. New Zealand Geological Survey

764   Paleontological Bulletin 36, 1-283.

765   Swart, P.K., 2015. The geochemistry of carbonate diagenesis: The past, present and future.

766   Sedimentology 62, 1233-1304.

767   Ullmann, C.V., Korte, C., 2015. Diagenetic alteration in low-Mg calcite from macrofossils: A review.

768   Geological Quarterly 59, 3-20.

769   Ullmann, C.V., Frei, R., Korte, C., Hesselbo, S.P., 2015. Chemical and isotopic architecture of the

770   belemnite rostrum. Geochemica et Cosmochimica Acta 159, 231-243.

771   Ullmann, C.V., Thibault, N., Ruhl, M., Hesselbo, S.P., Korte, C., 2014. Effect of a Jurassic oceanic

772   anoxic event on belemnite ecology and evolution. Proceedings of the National Academy of

773   Sciences of the United States of America 111, 10073-10076.

774   Urey, H.C., Lowenstein, H.A., Epstein, S., McKinney, C.R., 1951. Measurements of paleotemperatures

775   and temperatures of the upper Cretaceous of England, Denmark, and the southern United States.

776   Bulletin of the Geological Society of America 62, 399-416.

777   Veizer, J., 1974. Chemical diagenesis of belemnite shells and possible consequences for

778   paleotemperature determination. Neues Jahrbuch für Geologie und Paläontologie,

779   Abhandlungen 147: 91-111.

780   Visscher, P.T., Stolz, J.F., 2005. Microbial mats as bioreactors: populations, processes and products.

781   Palaeogeography, Palaeoclimatology, Palaeoecology 219, 87-100.

782   Voigt, S., Wilmsen, M., Mortimore, R.N., Voigt, T., 2003. Cenomanian palaeotemperatures derived

783   from the oxygen isotopic composition of brachiopods and belemnites: evaluation of Cretaceous

784   palaeotemperature proxies. International Journal of Earth Sciences (Geologische Rundschau) 92,

785   285-299.

786   Wanamaker, A.D., Baker, A., Butler, P.G., Richardson, C.A., Scourse, J.D., Ridgway, I., Reynolds, D.J.,

787   2009. A novel method for imaging internal growth patterns in marine mollusks: A fluorescence

788   case study on the aragonitic shell of the marine bivalve *Arctica islandica* (Linnaeus). Limnology

789   and Oceanography: Methods 7, 673-681.

790 Weiner, S., Addadi, L., 2011. Crystalization Pathways in Biomineralization. Annual Review of Materials

791   Research 41, 21-40.

792 Wierzbowski, H., 2004. Carbon and oxygen isotope composition of Oxfordian-Early Kimmeridgian

793   belemnite rostra: palaeoenvironmental implications for Late Jurassic seas. Palaeogeography,

794   Palaeoclimatology, Palaeoecology 203, 153-168.

795 Wierzbowski, H., Joachimski, M.M., 2007. Reconstruction of late Bajocian-Bathonian marine

796   palaeoenvironments using carbon and oxygen isotope ratios of calcareous fossils from the Polish

797   Jura chain (central Poland). Palaeogeography, Palaeoclimatology, Palaeoecology 254, 523-540.

798 Wierzbowski, H., Joachimski, M.M., 2009. Stable Isotopes, Elemental Distribution, and Growth Rings

799   of Belemnopsid Belemnite Rostra: Proxies for Belemnite Life Habitat. Palaios 24, 377-386.

800 Zachos, J., Pagani, M., Sloan, L., Thomas, E., Billups, K., 2001. Trends, Rhythms, and aberrations

801   inglobal climate 65 Ma to present. Science 292, 686-693.

802

803

804

805

806

807

808

809

810

Figure captions

812

813   **Fig. 1A-B) Structural and ultrastructural composition of belemnite rostra.** *Belemnitella mucronata*,

814   thin sections photographed under crossed polarizers. A) Cross section with pseudo-uniaxial cross

815   indicating radially arranged calcite fibres, red box refers to C. B) Longitudinal section with central

816   apical line and radiating fibres from the centre to the margin, stippled line refers to the position of

817   cross section shown in A. C) Idealized bundle of calcite fibres, each fibre contains a stack of

818   tetrahedral elements. D) SEM BSD image of the tetrahedral ultrastructure of *Megateuthis gigantea*,

819   dashed lines (I-IV) indicate section planes and corresponding reconstructions. Primary skeletal

820   framework is shown in blue, yellow and green whilst early diagenetic phase is shown in white and

821   red for the crystal boundaries. The basis of tetrahedrons points toward the centre of the belemnite

822   rostrum and its tip towards the rostrum margin i.e. the growth direction. E) Three dimensional

823   reconstruction of a single tetrahedron of the belemnite endoskeleton. F) Reconstruction of the

824   complex spatial arrangement of biogenic and early diagenetic phases. Colour code in lower right. G)

825   SEM image of a single complex tetrahedron (black line) with indication of structural elements.

826   Primary skeletal components: br = branch, trc = triradial centre, rf = reinforcement, ic = isopachous

827   crystallites. **(full page width; bw in print, colour in pdf)**

828

829

830

831

832

833

834

835

836

837   **Fig. 2A-B) SEM BSD images of *Megateuthis gigantea*.** A-B) Section perpendicular to the c-axes of

838   calcite fibres (section plane II in Fig. 1D-II). White stippled line indicate dissolution features (early

839   diagenetic), black stippled line indicate microstylolites ~~(late diagenetic)~~. **(full page width; bw in print,**

840   **colour in pdf)**

841

842   **Fig. 2A-B) SEM BSD images of *Megateuthis gigantea*.** A-B) Section perpendicular to the c-axes of

843   calcite fibres (section plane II in Fig. 1D-II). Blue stippled line indicate dissolution features (early

844   diagenetic), red stippled line indicate microstylolites ~~(late diagenetic)~~. **(full page width; bw in print,**

845   **colour in pdf)**

846

847

848

849

850

851

852

853

854

855

856

857

858

859

860

861

862

Fig. 3A-F) SEM BSD images of *Megateuthis gigantea*. A-E) Section perpendicular to the c-axes of calcite fibres. A) Triangular structures with a relatively thick outer, light grey margin of abiogenic early diagenetic cement and a small darker centre with branches giving rise to reinforcement structures representing the primary biogenic skeletal framework. B) Larger dark grey, organic rich triangular elements belonging to the biogenic skeletal framework, partly with light grey central abiogenic calcite filling of variable sizes. Branches are often short and cut off at variable distances from the centre. C) Some smaller and a few larger biogenic skeletal elements with cut off branches (lower arrow) and reinforcement structures (upper arrow). Note the variable expression of early diagenetic crystallites with sheaths of remnant organic matter. D) Close up of larger, biogenic skeletal elements and abiogenic isopachous calcites coated by remnants of organic matter within the brighter outer margin. Central portion of the biogenic skeletal elements shows abiogenic crystal; arrows point to dissolved branches. E) Centre of biogenic skeletal element completely filled with abiogenic bright calcite leaving only a thin dark inner margin. F) Same specimen, section subparallel to the c-axes showing a homogenous central portion ("trunk" – white line) of pyramidal morphology rich in intracrystalline organic matter surrounded by inclined isopachous calcite crystals coated by remnants of organic matter. This overall pattern results in an "Christmas mas tree like" structure (compare with Fig. 1D). **(full page width; bw in print and pdf)**

Fig. 4A-E) *Megateuthis gigantea*, EBSD map with colour code in sections perpendicular to the c-axes of the fiber bundles. Same colours represent same crystallographic orientations. In A and B angular deviation from blue to red is up to 40°, in D angular deviation is 2°. A) Overview map showing the bundling of fibres with identical orientation of a-axes, black frame indicates area for close up in B; blue frame refers to Fig. 5A-C. B) Close up map, within one bundle blue tinted fibres are mainly neighboured by other blue fibres, red tinted fibres are surrounded by red fibres. C) Close up ~~to demonstrate slight~~ documenting minor angular deviation within one fibre (compare with D). D) Map of a single fibre with an angular deviation of 2° from blue to red, showing a slight systematic shift of axes orientation. E) Pole-plots of c-axes {001} and a-axes {010} from all fibres shown in A, all c-axes show nearly the same orientation while the a-axes demonstrate the bundled structure of the rostral fabric which may have improved the stability of the skeletal structure. **(full page width; bw in print, colour in pdf)**

913   **Fig. 5A-F) Transmitted light, polarized light and cathodoluminescence**. Thin section of *Megateuthis*

914   *gigantea*, A-C refer to the blue frame in Fig. 4A, D-F are close ups (black frame in A) A and D) TL

915   image perpendicular to the c-axes of calcite fibres, filigree biogenic skeletal framework is indicated

916   by the dark tinted structures, primary porosity is represented by the abiogenic translucent calcites.

917   Note banded distribution of calcite fibre domains relating to larger and smaller organic-rich biogenic

918   skeletal elements, single fibres may contain a central portion of transparent calcite of varying size,

919   bundling of adjacent calcite fibres is indicated by the same orientation of the triangles. B and E)

920   Uniform extinction (orientation) of adjacent fibres under crossed polarizers. C and F) CL of abiogenic

921   calcite portions show a dark blue, intrinsic luminescence (pure stoichiometric calcite), CL of the

922   biogenic skeletal framework show light blue luminescence. **(full page width; bw in print, colour in**

923   **pdf)**

924

925

926

927

928

929

930

931

932

933

934

935

936

937

938 **Fig. 6) Electron microprobe data for *Megateuthis gigantea*.** A) Overview BSE map B) Shows higher

939 Mg concentrations within the triangular areas dark in BSE images and a lower Mg concentration in

940 the surrounding area bright in BSE images. C) Shows higher P concentrations within the triangular

941 areas dark in BSE images and a lower P concentration in the surrounding area bright in BSE images.

942 D) Shows lower S concentrations within the triangular areas dark in BSE images and higher S

943 concentrations in the surrounding region bright in BSE images. **(full page width; bw in print, colour**

944 **in pdf)**

945

946

947

948

949

950

951

952

953

954

955

956

957

958

959

960

961

962

963

964 **Fig. 7) Fluorescence microscope images for *Megateuthis gigantea*.** A) Transmitted light shows

965 brownish triangular structures, rich in organic matter and dark in BSE images, partly with central

966 translucent areas (compare with Fig. 1D section plane IV, Fig. 3D, E, 5A, D). B) Shows brighter

967 fluorescent triangular area compared to the in transmitted light translucent calcite. **(full page width;**

968 **bw in print, colour in pdf)**

969

970

971

972

973

974

975

976

977

978

979

980

981

982

983

984

985

986

987

988

989

990 **Fig. 8) Confocal laser fluorescence microscopy images of *Megateuthis gigantea*. A)** CLFM images

991 showing fluorescence in far-red light (λ = 664 to 696 nm). B) CLFM images showing fluorescence in

992 visible green light (λ = 505 to 539 nm). C and D) CLFM images showing fluorescence in visible red light

993 (λ = 589 to 621 nm). Triangular structures visible in other imaging techniques (Fig. 3, 5-7) do not

994 fluoresce as brightly as cracks (B) or early diagenetic calcite (Fig. 3) separating the triangles (A, B, C,

995 D). D) Higher magnification shows some brighter fluorescing calcite between the triangular elements

996 dark in BSE images (Fig. 1, 3). Brightly fluorescent early diagenetic calcite separating triangles ~~also~~

997 ~~contains~~is enriched in ~~elevated~~ S (Fig. 6)~~,~~). ~~which may support inclusion of S rich humic substances as~~

998 ~~the cause of fluorescence.~~ **(full page width; bw in print, colour in pdf)**

1016 **Fig. 9) Three-dimensional visualization of the filigree biogenic framework**. Synchrotron radiation

1017 based tomographic visualization of a sub-volume of the rostrum of *Megateuthis gigantea*. Specimen

1018 was scanned with an isotropic voxel size of 0.74μm. A) Multi-planar image of a sub-domain of the

1019 original dataset with dimensions of 447x592x663 voxels, triangular elements dark in BSE images

1020 appear here as dark elements due to reduced densities. B-D) Volumetric renderings of the same sub-

1021 domain with variable rendering settings. **(full page width; bw in print, colour in pdf)**

1022

1023

1024

1025

1026

1027

1028

1029

1030

1031

1032

1033

1034

1035

1036

1037

1038

1039

1040

1041

Supplementary Figures

1061 **Fig. 1) Examples of the filigree framework from other belemnite species.** A-B) *Gonioteuthis*

1062 *quadrata*, A) shows the Becke line outside of the triangular area with a relatively larger distance

1063 between the sample and objective. B) ~~Shows~~ Image shows the Becke line within the triangular area

1064 while the distance between the sample and the objective was reduced, accordingly the triangular

1065 area (dark in BSE; ~~(~~Fig. 3~~)~~) has a lower optical relief. C-D) *Belemnitella mucronata*, C) thin section

1066 under polarized light, D) same area under CL showing microfractures filled with Mn-rich calcite

1067 tracing the outline of triangular elements (encircled). **(full page width; bw in print, colour in pdf)**

1081   **Fig. 2) SEM BSD images of *Megateuthis gigantea*.** A-F) Section plane parallel to the c-axes of calcite

1082   fibres. A-C) stepwise enlargement of a particular area. D-F) stepwise enlargement of a particular

1083   area. A and D give the impression of a concentric arrangement of distinct darker and brighter layers

1084   (black frames enlarged in B and E), arrow in D point to an organic rich layer (laminae obscura sensu

1085   Müller-Stoll, (1936)). B and E) Allow the recognition of single darker structures of tetrahedral

1086   morphology with their tips pointing towards the outer margin of the belemnite rostrum, i.e. the

1087   growth direction (black frames enlarged in C and F). C and F) show the intricate framework of

1088   biogenic (dark) and abiogenic (light) carbonate phase within the rostrum, larger dark grey, triangular

1089   elements belonging to the biogenic skeletal framework, partly with light grey central abiogenic

1090   calcite filling of variable size. **(full page width; bw in print, colour in pdf)**

1091

1   **Evidence for a composite organic-inorganic fabric of belemnite rostra:**

2   **Implications for palaeoceanography and palaeoecology**

3

4   Hoffmann, R.[1], Richter, D.K.[1], Neuser, R.D.[1], Jöns, N.[1], Linzmeier, B.J.[2], Lemanis, R.E.[1], Fusseis, F.[3],

5   Xiao, X.[4] and Immenhauser A[1]

6

7   [1] Department of Earth Sciences, Institute of Geology, Mineralogy, and Geophysics; Ruhr-Universität

8   Bochum, Universitätsstrasse 150, 44801 Bochum, Germany

9   Corresponding author. E-mail address: rene.hoffmann@rub.de (R. Hoffmann), phone number: +49-

10   234-3227769

11   [2] Department of Geoscience, University of Wisconsin – Madison, 1215 West Dayton St, Madison,

12   Wisconsin, USA

13   [3] School of Geosciences, The University of Edinburgh, Grant Institute, King's Buildings, West Mains

14   Road, Edinburgh, UK EH9 3JW

15   [4] Advanced Photon Source, Argonne National Laboratory, 9700 S. Cass Ave., Lemont, IL, 60439 USA.

16

17

18

19

20

21

22

23

24

25

26

27   **Abstract**

28

29   Carbonate skeletons of fossil marine organisms are widely used to reconstruct palaeoceanographic

30   parameters. Specifically, the geochemistry of Jurassic and Cretaceous belemnite rostra is traditionally

31   interpreted to represent near sea-surface seawater properties. More recently, an increasing number

32   of workers, have reported significant scatter in geochemical data (e.g., δ^{18}O, δ^{13}C, element/Ca ratio)

33   when comparing rostra from the same stratigraphic level or within a single belemnite rostrum. This

34   scatter is not explained by differential diagenetic overprint alone. Here we report petrographic

35   evidence on the primary ultrastructure of rostra of *Megateuthis* (Middle Jurassic) and *Belemnitella*

36   and *Gonioteuthis* (Late Cretaceous). The biogenic ultrastructure consists of a filigree framework of

37   triaxial branches and tetrahedrons of variable size forming a honeycomb-like network. Data

38   presented here suggest that these rostra yielded as much as 50 to 90% primary pore space. On the

39   level of a working hypothesis - and in analogy with modern cephalopods - we propose that the pore

40   space was formerly filled with body fluid and/or organic compounds during the life time of these

41   organisms. Intra-rostral porosity was post mortem occluded by earliest diagenetic isopachous calcite

42   cements of a non-biogenic origin. These may have been precipitated due to increased alkalinity

43   related to the decay of organic matter. If this holds true, then the resulting fabric represents a

44   composite biogenic/abiogenic structure. In order to optically separate the two calcite phases forming

45   a single calcite fibre, we employed a wide range of state-of-the-art analytical tools to thin sections

46   and ultra-thin sections of well-preserved specimens. Pending a verification of these well-supported

47   ultrastructural data by means of high-resolution geochemical analyses from biogenic and abiogenic

48   phases, we suggest that these findings have significance for those using belemnite rostra as archives

49   of their palaeoenvironment.

50

51   **Keywords:** belemnite, ultrastructure, carbonate archive, diagenesis, Jurassic-Cretaceous

52

1.   Introduction

The ultrastructure of recent biogenic carbonates is of great interest for those concerned with biomineralization research in general (Weiner and Addadi, 2011; Goetz et al., 2011), those studying the primary biogenic skeletal structures of fossil skeletal hardparts (e.g., Coronado et al., 2013), and for palaeoceanographers exploring these materials for their bearing on past climate dynamics (Saelen, 1989; Cochran et al., 2003; Parkinson et al., 2005; Jarvis et al., 2015; Immenhauser et al., 2016). Whereas the tests of planktonic and benthic foraminifera and coccoliths are important archives of open marine environments throughout the Cenozoic and beyond (e.g., Zachos et al., 2001), much of what is known about Cretaceous and Jurassic palaeoceanography has been deduced from the geochemical archive of the calcareous rostra of extinct cephalopods, specifically belemnites (Dutton et al., 2007). Reasons for the wide use of these archive materials include their abundance in the fossil record, the diagenetically stable low-Mg calcite mineralogy of rostra (Veizer, 1974; Saelen, 1989), and the broad palaeobiogeographic distribution of belemnites in the marine Boreal and Tethyan realms, (e.g., Urey et al., 1951; Voigt et al., 2003; Wierzbowski, 2004; McArthur et al., 2007; Dutton, 2007; Price and Page, 2008; Wierzbowski and Joachimski, 2009; Price et al., 2009 2011; Li et al., 2012, 2013). As with all biogenic carbonates, however, these archives undergo post mortem diagenetic alteration, representing a major obstacle in carbonate research (Swart, 2015).

Characteristic geochemical patterns and fabrics in biogenic carbonate hardparts have been used to test for example molluscs (e.g., Cochran et al., 2003, Sessa et al., 2015, Immenhauser et al., 2016), brachiopods (Parkinson et al., 2005), or foraminifera (e.g., Huber and Hodell, 1996; Kozdon et al., 2011) for evidence of diagenetic alteration. In the case of ammonites, the degree of preservation of nacre tablets provides evidence with regard to the preservation of these exoskeletons, to name one example (e.g., Cochran et al., 2010). With regard to belemnite rostra, the observation of an intact fibrous microfabrics in thin sections and polished rock surfaces in combination with cathodoluminescence is commonly used to identify well-preserved belemnite rostra (Rosales et al., 2001). In contrast, cloudy areas, exfoliation, fractures, stylolites, or boring traces are interpreted as

79   evidence for post mortem alteration (Saelen, 1989; Li, 2011; Benito and Reolid, 2012). A rigorous

80   discussion of screening techniques, including trace-element concentrations, and isotopic ratios

81   applied to biogenic low-Mg calcite macrofossils, has been provided by Ullmann and Korte (2015).

82   Similarly, a "best practice" approach for the interpretation of mollusc and brachiopod carbonate

83   archives was presented by Immenhauser et al. (2016).

84   The ultrastructure of belemnite rostra was first studied by Müller-Stoll (1936). This author

85   described organic-rich (laminae obscura) and carbonate-rich (laminae pellucidae) concentric growth

86   rings. Both of these were later shown to be calcitic but differ due to variable amounts of occluded

87   organic matter (Saelen, 1989). Growth rings are made up by fibrous calcite crystals radiating from a

88   central zone called apical line (Richter et al., 2011) forming what seems to be a low-porosity fabric

89   (Saelen, 1989 and references therein; Fig. 1A-C). Single fibres (= radial structures of Saelen, 1989) can

90   be arranged in bundles traversing the concentric growth layers. Each fibre thickens outwards and

91   shows a sub-fibrous framework potentially first proposed - but not further explored - by Saelen

92   (1989, Fig. 15a).

93   Belemnites are traditionally considered to secrete their endoskeleton in oxygen isotope

94   equilibrium with ambient seawater (e.g., Anderson et al., 1994; Price and Sellwood, 1997; Voigt et

95   al., 2003; Price et al., 2009; Wierzbowski and Joachimski, 2007, 2009). The main argument brought

96   forward is commonly the presence of what are considered cyclical oxygen isotope patterns

97   interpreted as seasonal seawater temperature variations (Urey et al., 1951). The PeeDee belemnite

98   used in Urey´s study was considered as well-preserved based on the compact fabric and the optical

99   features of the calcite crystals (but see Li, 2011 for discussion). The assumption of equilibrium

100   precipitation was further supported by data sets from recent cephalopods including *Nautilus*, *Sepia*,

101   and *Spirula* precipitating their skeletal hardparts in near-equilibrium with $\delta^{18}O_{seawater}$ (Lukeneder et

102   al., 2010). In contrast to this traditional view, there is an increasing amount of evidence suggesting

103   that belemnite rostra are problematic archives of their palaeoenvironment (see Immenhauser et al.,

104   2016 for detailed discussion). For example, Price et al. (2015) reported an offset of about 5°C

4

105 between the aragonitic phragmocone and the calcitic rostrum of a single specimen of

106 *Cylindroteuthis*. This offset was regarded as vital effect but it remains unclear whether the

107 temperatures derived from the aragonite are too warm or from the calcite too cool. Similarly, high

108 intra-rostral variability of elemental (Ca, Mn, Mg, Fe, Sr) and isotopic (δ^{18}O, δ^{13}C) composition, the

109 latter with a scatter of up to 2‰, has been reported from belemnite rostra lacking evidence for

110 diagenetic alteration (Podlaha et al., 1998).

111   The significant discrepancy of these data sets forms a strong motivation for a reconsideration of

112 belemnite rostra as archives of their palaeoenvironment. Here, we report data from a wide set of

113 state-of-the-art analytical infrastructure applied to thin- and ultra-thin sections of exceptionally well-

114 preserved Jurassic and Cretaceous belemnite rostra. The following aims guided this paper: First, to

115 present well-constrained petrographic evidence for the complex primary biogenic framework of

116 these rostra; second, to document evidence that points to the highly porous nature of this biogenic

117 framework; third, to assess the relative proportion between primary skeleton and porosity; fourth, to

118 discuss the timing and nature of the pore-filling calcites phase. Evidence reported here has

119 significance for the interpretation of proxy data from ancient belemnite rostra and forms the

120 foundation of a detailed, high-resolution geochemical study that will be in the focus of forthcoming

121 work.

122

123 **2.   Materials and Methods**

124 *2.1. Belemnites*

125

126   Thin sections (30 μm) and ultra-thin sections (< 10 μm) of two well-preserved orthorostra of

127 *Megateuthis gigantea* (Schlotheim, 1820) from the Middle Jurassic and one specimen of *Belemnitella*

128 *mucronata* (Schlotheim, 1813) and *Gonioteuthis quadrata* (Blainville, 1827) from the Upper

129 Cretaceous were studied. Specimens of *Megateuthis* were collected in Bajocian marly limestone

130 deposits from southern Germany. *Belemnitella* rostra are from the late early Campanian (*mucronata*

131   Zone), and *Gonioteuthis* from the early Campanian *lingua/quadrata – gracilis/mucronata* Zone from

132   northwestern Germany. *Gonioteuthis* and *Belemnitella* rostra were embedded in calcareous (65-90%)

133   epicontinental shelf deposits of the Misburg Formation (Niebuhr, 1995; Niebuhr et al., 2007).

134   Specimens did not display evidence for exfoliation nor did they show boring traces of the surfaces of

135   rostra. Specimens were sectioned along their long axis in a marginal position and perpendicular to

136   the c-axis of their calcite fibres. One section cuts the rostrum of *Megateuthis* perpendicular to the

137   long axis.

138

139   *2.2. Methods*

140

141   Surfaces of thin sections were chemo-mechanically etched using colloidal silica (OP-S) for 5-15

142   minutes to reduce surface irregularities on an atomic scale (Massonne and Neuser, 2005) and coated

143   by a thin carbon layer. All coated thin sections have been studied under a high-resolution field

144   emission scanning electron microscope (HR-FESEM) type LEO/ZEISS 1530 Gemini using a backscatter

145   detector (BSD) at the Ruhr-Universität Bochum, Germany (Figs. 1-3).

146   Crystallographic orientation of belemnite calcite fibres was determined by electron

147   backscattered diffraction (EBSD; Nordlys, OXFORD Instruments). The data acquisition and analysis

148   was performed using the software packages AZtec and Channel 5 by Oxford Instruments (Fig. 4). The

149   scanning electron microscope (SEM) was operated at beam energy of 20 kV, an aperture of 60 µm, a

150   working distance of 25 mm and a tilt angle of 70°. Thin sections were mapped at Bochum University

151   in the high-resolution mode using a grid matrix (1149x748 points) at a step width of 2.017 µm (Fig.

152   4A) and (543x266 points) at a step width of 1.652 µm (Fig. 4D) and for the single calcite fibre 50 µm

153   to reduce artefacts and increase the reliability of the data. The orientations of the crystals in the

154   individual maps were visualized using a rainbow colour coding ranging from blue over green and

155   yellow to orange and red, where identical colours indicate identical crystal axis orientations. For

156   visualizing the weak angular deviations in the crystal lattice in a single calcite fibre, we applied an

6

157 angular resolution of 2 degrees for the complete rainbow colour range. In addition, orientations of

158 the measured crystallographic axes were plotted into the lower hemisphere of a Schmidt net (Fig.

159 4E).

160 Rostra were further investigated under a cathodoluminescence microscope type HC1-LM by

161 Lumic equipped with a hot cathode (Neuser et al., 1996) and a digital camera system (DP73 by

162 Olympus) for recording digital images at Bochum. Beam energy of 14kV and a beam current density

163 between 5 and 10 µA/mm² were generally used for the CL-measurements. Integration times for CL-

164 spectra were commonly between 10 and 60 seconds (Fig. 5).

165 X-ray element distribution maps were acquired using a Cameca SX5FE field emission electron

166 microprobe at Bochum. The acceleration voltage was 15 keV with a probe current of about 80 nA and

167 a fully focused beam. The intensity of S Kα1 was recorded simultaneously on two wavelength

168 dispersive spectrometers equipped with LPET and PET analyzing crystals. The Mg Kα1 line was also

169 measured on two spectrometers (LTAP and TAP crystals), whereas P Kα1 was measured on a single

170 spectrometer equipped with a LPET crystal. The images were acquired in continuous stage scan

171 mode. They have a resolution of 2048 x 1536 pixel, and the dwell time was 17 ms per pixel (Fig. 6).

172 To test for the distribution of organic matter within the belemnite rostra, thin sections were

173 studied under a fluorescence microscope (Leica DM4500P) equipped with a mercury short-arc

174 reflector lamp coupled with a Leica EL6000 compact light source. We used the blue light filter set

175 producing bright green fluorescence images (filter set I3 for blue light excitation: excitation 450-490

176 nm, emission 515 nm, voltage 100-240 VAC and 50-60 Hz frequency; Fig. 7). Fluorescence microscopy

177 in the manner applied here is an optical tool to qualitatively document the spatial distribution of

178 organic matter in shells. Fluorescence reflects organic matter and less commonly crystal lattice

179 defects and solid inclusions in crystals. Further details of this method have been presented by

180 Wanamaker et al. (2009) and Ritter et al. (subm.).

181 Confocal laser fluorescence microscopy (CLFM) images on an uncoated *Megateuthis* mount

182 were made using a Bio-Rad MRC-1024 scanning confocal microscope at the W. M. Keck Laboratory

183   for Biological Imaging at UW-Madison (Fig. 8). The microscope was operated with a 40 mW laser at

184   wavelengths of 488 nm, 568 nm, and 647 nm. All three wavelengths were simultaneously rastered

185   across the sample. Naturally occurring compounds within the sample caused fluorescence at multiple

186   wavelengths. Images were collected through the following three emission filters: visible green light (λ

187   = 505 to 539 nm); visible red light (λ = 589 to 621 nm); and far-red light (λ = 664 to 696 nm).

188   In order to analyze the three dimensional filigree framework, synchrotron radiation based

189   micro-computed tomography was applied (Fig. 9). Data were collected at the bending magnet beam

190   line 2-BM at the Advanced Photon Source, Argonne National Laboratory, USA. A double multilayer

191   monochromator of 1.5% band-width provided 27.2 KeV X-rays. Images were collected in transmission

192   mode by a CCD camera behind the sample in the hutch configuration. The sample-detector distance

193   was set to 300 mm to collect quantitative phase contrast data. 1440 projections were acquired while

194   the sample was rotated over 180° in steps of 0.125°. A microtomographic data set with a size of 2048

195   x 2048 x 1948 voxels was reconstructed using a phase retrieval algorithm (Mokso et al., 2013).

196

197

198   **3.   Results**

199   *3.1 Optical-, cathodoluminescence-, fluorescence-, and confocal laser fluorescence microscopy (TL, CL,*

200   *FL, CFLM)*

201   Under transmitted light (TL), thin sections of rostra cut perpendicular to the c-axis of calcite

202   fibres reveal a banded distribution of calcite fibres containing brownish triangular elements of

203   variable size (Fig. 5A, D). Some of the larger fibres contain a triangular, organic-rich centre, with its

204   innermost domains occluded by translucent calcite. Bundling of neighbouring calcite fibres is

205   indicated by their subparallel orientation of their a-axis (Fig. 5D). A uniform extinction (orientation)

206   pattern of adjacent fibres under crossed polarizers is observed (Fig. 5B, E) and is in agreement with

207   EBSD data (Fig. 4A). Individual fibres display an undulatory extinction (converging or diverging c-axes)

208 under crossed polarizers. Calcite occluding space between organic-rich elements and fibre

209 reinforcement is translucent and contains little or no organic matter (Fig. 5D). Brownish, triangular

210 elements have a relatively low optical relief, compared to the surrounding translucent calcite with a

211 relatively higher optical relief (supplement Fig. 1A-B).

212 Three different luminescence patterns are observed under the cathodoluminescence

213 microscope (CL): (i) A light blue luminescence of the brownish, triangular elements (Fig. 5C, F); (ii)

214 dark blue, intrinsic luminescence of the translucent phase; (iii) locally, orange to red luminescent

215 fractures and microstylolites are observed. In rare cases, fractures retrace the triangular outline of a

216 fibre (Fig. 5C, F, supplement figure 1D).

217 Brownish triangular areas under transmitted light display light green fluorescence while the

218 translucent areas show a dark green fluorescence under the fluorescence microscope (FL).

219 Microfractures are darker under transmitted light compared to the triangular elements and show a

220 light green fluorescence (Fig. 7A-B).

221 Different fluorescence patterns under the CLFM reveals calcite domains visible in BSE (and

222 other) imaging techniques (Figs. 3, 5-7). Filled cracks fluoresce brightly in green and red wavelengths

223 (Fig. 8B-C). Domains that are dark in BSE do not fluoresce in CLFM (Fig. 8A-D). Bright domains in BSE

224 fluoresce brightly in CLFM at all wavelengths observed (Fig. 8A-D). Higher magnification reveals

225 brighter fluorescence between adjacent domains that appear bright in BSE (Fig. 8D).

226

227 *3.2 Scanning-electron microscopy equipped with a backscatter detector (SEM BSD)*

228 Images collected with the scanning electron microscope equipped with a backscatter detector

229 present important evidence for the presence of two calcite phases (dark and bright) of different

230 chemical compositions building the rostra studied. The brownish triangular areas under transmitted

231 light are dark in BSE. Thin sections cut perpendicular to the c-axis of the radiaxal fibrous calcite (Fig.

232   1D I-IV) reveal a complex framework, dark in BSE, surrounded by relatively brighter calcite (Figs. 1-3).

233   Cross sections of the majority of fibres are polygonal or, less often, honeycomb shaped with a tri-

234   radial (120°) symmetry representing an ultrastructure that has not been described in previous studies

235   (Figs. 1C-G, 3A-E). Individual fibre diameters vary between 10-80 µm. Calcite fibres terminate at

236   individual concentric growth layers that also form the nucleation site for the overlying, next fibre

237   generation, displaying increasing thicknesses and occurring in increasing numbers towards the outer

238   portions of the rostrum (Fig. 1A-D). Brighter area in BSE are more likely to be composed of near-

239   stoichiometric $CaCO_3$ with higher average atomic masses (mainly Ca), whereas excess C, P, Mg, or S

240   will lower the average atomic mass. Accordingly, areas with decreasing amount of Ca and increasing

241   amounts of C, P, Mg or S are darker.

242   Four section planes are presented to describe the intricate bio-composite mineral present

243   within a single fibre. The following description distinguishes between the darker framework (i), i.e.,

244   micrometre-thick branches terminating in wall-like reinforcements and (ii) tri-radial central portions;

245   and brighter fabric (iii) consisting of calcite crystals forming isopachous cement layers with individual

246   crystallites coated by submicrometre thick layers of matter darker in BSE (Fig. 1G). In all sections, we

247   observed isopachous calcite crystals oriented perpendicular to the inner dark walls (Fig. 3A-E).

248   Section plane I consists of three simple, dark in BSE branches of variable lengths. Often, these

249   branches exhibit reinforcements of variable lengths and thicknesses (about 1 micrometre) and

250   increasing widths towards neighbouring branches (Figs. 1D-I, 3A). Conversely, reinforcements being

251   connected to neighboring triangles are rarely observed. Section type II is characterized by an

252   enlarged, dark in BSE central element of variable diameter (2-30 µm, Figs. 1D-II, 3C). Some of the

253   larger central elements display an inner zone with additional tri-radial structures comprising of

254   smaller, isopachous, brighter in BSE area calcite crystals rotated by 60° relative to outer branches

255   (Figs. 1D-III, 3D; section type III). Section type IV represents the most complex fabric. Here, the inner

256   portions of larger central elements display alternating darker and brighter in BSE areas (Figs. 1D-IV,

257 3E). Generally, enlarged central elements correlate with a shortening of corresponding, darker

258 branches.

259 Thin sections cut parallel to the c-axis of the radiaxial fibrous calcite reveal an framework dark in

260 BSE of triangular shaped elements with their tips pointing towards the outer margin of the rostrum

261 (Fig. 1C-D, supplement Fig. 2). Lighter and darker areas within a single calcite fibre show their

262 composite nature. Lighter and darker areas within concentric growth rings, as visible in transmitted

263 light, depend on the number and size of these elements. Higher magnification reveals a homogenous

264 central portion ("trunk" – white line) of pyramidal morphology dark in BSE surrounded by inclined

265 isopachous calcite crystals coated by material dark in BSE. This overall pattern results in a "Christmas

266 tree like" structure (Fig. 3F). The dark framework forms the substratum upon which an isopachous,

267 translucent calcite phase nucleated (Fig. 1D, G 2-3). The boundary surface between the framework

268 dark in BSE and the surrounding carbonates brighter in BSE is, in places, corroded and uneven (Fig.

269 2).

270

271 *3.3 Electron microprobe analysis (EMPA)*

272 The contrasting chemical composition of the two different calcite phases building these rostra is

273 also revealed by EMP data. Detailed WDS scans show that the strongest variability is displayed by

274 Mg, P, and S, whereas other elements are almost constant or present in amounts close to the

275 detection limit (e.g., SrO = 0.1-0.2 wt.%; FeO = <0.1 wt.%; MnO < 0.5 wt.%. X-ray element distribution

276 maps show a generally low concentration of the elements Mg (MgO = 0.3-0.4 wt.%), P (P_2O_5 = 0.1-0.2

277 wt.%), and S (SO_3 = 0.20-0.50 wt.%). The Mg- and P-content is slightly elevated in the darker,

278 triangular areas in BSE images (MgO up to 0.6 wt.%; P_2O_5 up to 0.25 wt.%) compared to the relatively

279 brighter areas in BSE images in the centre of larger tetrahedrons and their vicinity. Lowest Mg

280 concentrations were found along microfractures that display bright luminescence colours (MgO < 0.2

281 wt.%; Fig. 6B). Sulfur has a higher concentration in the brighter areas in BSE images (SO_3 up to 0.65

282 wt.%) and lower concentrations in the darker areas in BSE images (SO_3 = 0.20-0.50 wt.%; Fig. 6D). For

283 better comparison with BSE images from other samples and with the element distribution, BSE data

284 were obtained for the same field of view (Fig. 6A).

285

286 *3.4 Electron Backscattered Diffraction imaging (EBSD)*

287 Electron backscattered diffraction was used to document the biological controlled (sensu

288 Lowenstam and Weiner, 1989; Dupraz et al., 2009; Weiner and Addadi, 2011) formation of what is

289 here assumed to represent the primary biogenic skeletal carbonate. EBSD reveals a very low

290 variation of c-axes orientation of calcite fibres (Fig. 4A). The sub-parallel orientation of the c-axes

291 {001} is documented by their close fitting in the lower hemisphere of a Schmidt net (Fig. 4E, left plot).

292 A different characteristic is found for the crystallographic orientation of the a-axes {010} of calcite

293 fibres (Fig. 4E, right plot). All a-axes are aligned along a great circle whilst the colour code of the

294 according fibres is indicative of an arrangement in bundles. Adjacent fibres (10 to 100 fibres) share a

295 similar - if not identical - orientation (Fig. 4A-B). The majority of fibre bundles are characterized by

296 blue, green and red colour coding. Specifically, the spatial orientation of individual a-axes within a

297 single fibre bundle deviates by 20° or less from the bundle mean value. Variation in the orientation of

298 the c-axis of a single calcite fibre in the range of 1-3° was observed (Fig. 4D). As the angular

299 resolution from blue to red rainbow colour shown in EBSD maps (Fig. 4A-B) has a resolution of 50°,

300 minor angular deviations (<1°) are not visible in Fig. 4A-B.

301

302 3.5 *Synchrotron radiation based micro-computed tomography (SRµCT)*

303 Tetrahedral structures are visible in three dimensions in the tomographic dataset despite the

304 high signal to noise ratio and artefacts. There is a distinct difference in X-ray attenuation between the

305 inner tri-radial elements and the surrounding calcite.

306

4. Interpretation and Discussion

4.1 Reconstruction of the primary belemnite rostrum ultrastructure

309

310   Data presented here document a repeated pattern of triangular elements that seem to be

311   originally connected, building a concentric layered, highly complex, and porous framework. The

312   space between the former skeletal elements is interpreted as pore space probably filled by body

313   fluids or organic material during the life time of these organisms. The latter assumption is based on

314   analogous observations in the porous endoskeletons of recent *Sepia* (Sherrard, 2000; Guerra, 2006).

315   Referring to the high porosity observed in both, the belemnite rostrum and the sepiid cuttlebone, it

316   is important to note that these structures are not homologous (Fuchs 2012).

317   Accordingly, the belemnite rostra originally consisted of an organic-rich biogenic framework of

318   calcitic tri-radial tetrahedrons (triangular pyramids arranged perpendicular to the concentric layers

319   during lifetime). Tetrahedrons are elongated along their c-axis with the tip of the pyramid pointing

320   towards the precipitation site i.e., in growth direction towards the outer margin of the rostrum (Fig.

321   1C-D). Individual branches protruding from the edges of the tetrahedrons possess outer

322   reinforcements acting as stabilizers. The central portion of the tetrahedrons may yield a channel-like

323   cavity (Fig. 1D III-IV). Organic membranes at which nucleation of the tetrahedrons may have started

324   and stopped are not preserved. However, it seems likely that such membranes were present because

325   the bases of the tetrahedrons follow a concentric layer. Structurally, the bundling of the tri-radial

326   elements forms a simple honeycomb-like framework in which the terminations of branches of

327   adjacent elements are connected. The mechanical stability of the honeycomb structure is enhanced

328   by reinforcement walls (Figs. 1D, G, 3C).

329   Based on the variable dimensions of skeletal elements seen in thin sections, intra-rostral pore

330   space was visually estimated to range between 50-90% of the total rostrum (Fig. 3A: 90% pore space

331   and 10% skeletal elements; Fig. 3B; 50% pore space and 50% skeletal elements). In this context, the

332   observation that pore space is not limited to the apical line region but is present across the bulk

333   rostrum is important. The secretion of a porous, but mechanically stable orthorostrum is probably

334   best seen in the context of a considerable reduction of energy and building material required to form

335   this structure compared to a massive endoskeleton (Sherrard, 2000). Strict biological control, i.e. in

336   the presence of organic templates (Chateigner et al., 2000; Richter et al., 2011), over the

337   precipitation of primary skeletal elements is demonstrated by a systematic arrangement of adjacent

338   elements into bundles of similar or identical orientation of their crystallographic a-axes. This

339   configuration results in a much higher mechanical load capacity and torsion stiffness of the

340   framework of the rostrum.

341   Alternating concentric Ca-rich (brighter; laminae obscurae) and C-rich layers (darker; laminae

342   pellucidae) of Müller-Stoll (1936) are related with the banded distribution of larger and smaller

343   organic-rich triangular elements of the primary skeletal structure of the belemnite orthorostrum (Fig.

344   1D, supplement Fig. 2). These layers potentially indicate differences in calcite precipitation rates.

345   Based on petrographic and ultrastructural evidence, the Mg and Ca elemental concentrations of the

346   rostrum, the lack of secondary micro-dolomite, and the absence of blotchy luminescence, the widely

347   held assumption of a primary low-Mg calcite mineralogy for the studied belemnite rostra is

348   confirmed (see discussion in Richter et al., 2003).

349

350   *4.2 Early and late diagenetic processes*

351

352   The presence of a highly porous primary rostrum architecture during the life time of the

353   belemnite organism as proposed here, is in contrast to the dense fabrics observed in rostra collected

354   in Mesozoic sedimentary successions (Fig. 1A-B). Hence, the diagenetic pathway from porous to

355   dense fabrics deserves attention. The marine diagenetic alteration of biominerals is initiated directly

356   after the death of a carbonate-secreting marine organism when metabolic processes come to a halt.

357   At this early stage, organic matter outside of the orthorostrum (i.e., the belemnite animal itself) and

358   in the pore space of rostra and between biominerals decomposes (Saelen, 1989), triggering a series

359   of complex bio-chemical processes. Essentially, decomposition of organic matter is mediated by

360   microbial activity, and given the abundance of marine microbial life, there is no reason to assume

361   that this would have been different in the case examples studied here.

362   Microbial metabolic products, the presence of microbial "mucus" (extracellular polymeric

363   substance) and charged surfaces represented by microbial bodies influence the micro-environment

364   in intra-rostrum pore space by altering the balance between more reduced and more oxidized forms

365   of carbon as previously summarized under the term "alkalinity engine" (Dupraz et al., 2009).

366   Specifically, Visscher and Stolz (2005) subdivided microbial species into 5-7 groups ("guilds") having a

367   similar metabolism. Some of these promote carbonate precipitation (e.g., cyanobacteria, sulphate

368   reducers), whilst others favour dissolution (e.g., aerobic heterotrophs, fermenters). Dupraz et al.

369   (2009) documented that the balance of microbial metabolic activities directly influences carbonate

370   precipitation or, vice versa, dissolution. Initial microbial decomposition of organic matter may result

371   in the production of organic acids lowering the pH-values in the pore space (Berner et al., 1978),

372   enhancing intra-orthorostrum dissolution of biominerals (Fig. 2).

373   As soon as the bulk of organic matter is decomposed, alkalinity is increased due to microbial

374   metabolic products enhancing the precipitation of carbonate minerals (intrinsic

375   organomineralization) leading – in the view of the authors - to the formation of the translucent,

376   isopachous calcite crystals that occlude primary pore space in rostra (Fig. 2). Obviously, any

377   assumption regarding microbial processes in these ancient carbonates must remain speculative.

378   Nevertheless, following the basic concepts laid out in Dupraz et al. (2009), we tentatively assume

379   that a first phase of decomposition was dominated by aerobic heterotrophy, sulphide oxidation, and

380   fermentation decreasing the saturation index and resulting in the corrosion of skeletal elements in

381   the belemnite rostrum. Evidence for this comes from micro-corrosion features at the outer surfaces

382   of the primary skeletal framework forming the substratum upon which the pore-filling, secondary

383   calcite phase nucleates (Fig. 2).

384   The nucleation and precipitation of the secondary calcite phase (Fig. 1D, G, 2-3) was possibly

385   dominated by sulphate reduction increasing the saturation index and hence favoring precipitation of

386      $CaCO_3$. During crystals growth, remnants of belemnite organic matter combined with microbial

387   mucus were likely trapped between single crystals or at the growth front of crystals and delineate

388   crystal boundaries. Specifically, the growth of fibrous calcitic crystals will proceed as long as growth

389   rate, fluid supersaturation, and temperature are low enough to discourage spontaneous nucleation

390   (Oti et al., 1989). Similar processes have been described from extant echinoderm endoskeletons that

391   share a comparable amount of primary porosity with the described belemnite orthorostra (Richter et

392   al., 2003).

393   During this early stage of diagenetic evolution, the rostra most likely preserved their original

394   morphology due to the biogenic calcite framework and abiogenic calcite progressively occluding

395   former pore space preventing, in combination, a collapse of the rostra. The directly comparable, dark

396   blue intrinsic luminescence of the translucent secondary outer calcite layer and the calcite infill of

397   central pore space of many of the larger triangles (Figs. 3D-E, 5A, D, 6) suggest that both phases

398   precipitated from one fluid, or different fluids with near-identical geochemistry. This is, of course,

399   within the limitations of the geochemical resolution of the cathodoluminescence method and with

400   reference to elements that affect luminescence patterns (e.g., Mn^{2+}, Fe^{2+} and REE; see discussion in

401   Barbin 1991, 1993; Ritter et al., 2015). Conversely, the organic matter-rich triangles display a

402   moderately brighter blue luminescence pattern (Fig. 5C, F). This feature is best explained by calcite

403   lattice deformation due to the incorporation of organic matter into the crystal lattice

404   (intracrystalline) and is not necessarily indicative of a different geochemical composition. This

405   concept is supported by x-ray diffractometry (Richter et al., 2011) documenting that the fibrous

406   fabric of the belemnite rostra, lacking late diagenetic Mn-rich cements, is composed of

407   stoichiometric or near-stoichiometric calcites (d (104) = 3.030 to 3.035 Å).

408   A late diagenetic (burial) stage of rostra is documented by dissolution and compaction features

409   as indicated by microfractures and microstylolites (Figs. 2, 5C, F; Rosales et al., 2004a, b). The

410   circulation of Mn^{2+}-rich fluids caused the precipitation of a late calcite phase that occludes fractures

411   and fissures. In some cases this late phase yields a bright luminescence and is zigzag or triangular

412   shaped, tracing the morphology of the triangular biominerals (Fig. 5C).

413

414   *4.3 Implications for the function of the rostrum*

415

416   It is generally accepted that the belemnite rostrum acts as a counterweight to the soft body.

417   Based on the observation of a high primary porosity (see also Spaeth, 1971, 1973, 1975; Ullmann et

418   al., 2015), this interpretation requires renewed consideration. Rostra are commonly considered to

419   have the same density as inorganic calcite crystals, ranging from 2.5-2.7 g/cm³.

420   *Sepia*, the closest living relative of the extinct belemnites, incorporates a total of 10-40% organic

421   matter in its cuttlebone and comparably high amounts of intracrystalline organics were observed for

422   the biogenic belemnite orthorostrum. Accordingly, ignoring open pore space, a reduced density of

423   the biogenic belemnite calcite of about 2.4 g/cm³ (10% organic) − 2.0 g/cm³ (40% organic) results.

424   Assuming that liquid or extracrystalline organic matter (1.03 g/cm³) - with density comparable to that

425   of seawater (1.026 g/cm³) - filled up the pore space of living belemnite rostra, an overall density of

426   the rostrum ranging between roughly 1.7-1.1 g/cm³ (mean 1.4 g/cm³) is tentatively assumed on the

427   level of a working hypothesis. If these assumptions hold true, then the belemnite rostrum had a

428   cumulative density that is significantly lower than that of stoichiometric calcite. Therefore, questions

429   regarding the locomotion of belemnites result.

430   A possible analogue may come from a structure reported from a modern onychoteuthid squid

431   (*Onykia*) that has remarkable morphological similarity to the *Megateuthis* rostrum. *Onykia* has a

432   purely organic rostrum that due to its very low density does not act as a counterweight for the soft

433   body. It is assumed that it supports the posterior part of the mantle and fins (= axial stability in

434   Bizikov and Arkhipkin, 1997 and Arkhipkin et al., 2015). A function as a muscle attachment structure

435   for belemnite rostra was first put forward by Stevens (1965). Direct evidence for the presence of fins

436 in belemnites has recently reported by Klug et al. (2015), favouring a squid-like high speed swimming

437 mode of life for Jurassic belemnites. Noteworthy to report here, is the case of belemnites

438 (*Chitinoteuthis*) with a non-calcified rostrum (Müller-Stoll, 1936).

439

440 **5 Open questions and suggestions for future research**

441 5.1. Paragenesis of porosity-occluding calcite phase

442   Within individual belemnite rostra, data presented here differentiate: (i) a biogenic, highly

443 porous skeletal framework secreted during the life time of the organism; (ii) an inorganic or

444 organomineralic – arguably early diagenetic - calcite phase occluding the pore space of the biogenic

445 framework; and (iii) a late diagenetic, burial, Mn-rich carbonate phase filling fissures and larger

446 cracks within the rostra. Assuming that the above-discussed paragenetic succession is valid, a series

447 of open questions result. In the view of the authors, it is at least conceivable that portions of the

448 rostral pore space were occluded during the life time of the belemnites (remote biomineralization

449 sensu Hücker and Hemleben, 1976; Chinzei and Seilacher, 1993; Seilacher and Chinzei, 1993). If this

450 holds true, then the paragenetic sequence of primary framework and secondary infill calcite is even

451 more complicated than presented here and gradual in nature. Moreover, individual growth

452 increments within rostra are then not representative of specific correlative time intervals.

453 Specifically, each growth increment then represents a complex composite structure of paragenetic

454 phases representing temporally different stages in the belemnite ontogenetic cycle. Obviously, this

455 would render the interpretation of time series belemnite geochemical data difficult. Evidence against

456 a biogenic infill of the skeletal pore space by remote biomineralization sensu Seilacher and Chinzei

457 (1993), however, may or may not come from the presence of a corroded outer surface of what is

458 considered the primary skeletal ultrastructure of these rostra (Fig. 2). It seems difficult to argue that

459 intra-rostrum body fluids became corrosive at some stage during the life time of the belemnite

460 animal. Clearly, these questions require further detailed work.

461

5.2 Primary skeletal ultrastructure and preservation of organic matter

The authors acknowledge the fact that despite the very detailed information regarding the belemnite ultrastructure shown here, our study lacks direct evidence for a primary biogenic origin of the complex, highly porous framework and the subsequent cementation by an early diagenetic calcite phase. Open questions, however, remain. Specifically, the significance of preserved organic matter in the biogenic belemnite calcite deserves attention. In the following, we present several lines (petrographic, optical, and geochemical data) of circumstantial evidence suggesting the presence of preserved organic matter.

The sector-wise systematic arrangement of triangular elements - with their a-axis being oriented subparallel to parallel (Figs. 3A-C, 4A-B, 5A, D) - in bundles, indicate a biologically controlled origin (Lowenstam and Weiner, 1989) of these fabrics. The primary belemnite rostrum ultrastructure is brownish (Figs. 5A, 7A) in thin sections under transmitted light and has a relatively low optical relief. According to Ullmann et al. (2014), brownish areas in thin sections of biogenic carbonates are indicative of remnant organic matter (C_{org}). Under the cathodoluminescence- and fluorescence microscope, the primary filigree belemnite framework shows a light blue luminescence (CL) and light green fluorescence (FL). According to Wanamaker et al. (2009) and Pérez-Huerta et al. (2008), fluorescence in biominerals is triggered by organic macromolecules associated with chitin polysaccharides and proteins. Dark fluorescence patterns commonly refer to portions of the skeletal hardparts that are relatively depleted in organic matter. Bright green fluorescence patterns typify areas with increased amount of organic matter (Wanamaker et al., 2009).

Primary skeletal structures display darker colours in SEM-BSE images. Electron microprobe analyses revealed that the biogenic skeletal calcites contain more P and Mg but less S compared to what is here considered an early diagenetic, pore-filling calcite phase. Higher concentrations of P (Fig. 6C) may be related to the presence of organic matter. Arguments for this have been presented by

487   Longinelli et al. (2002, 2003) and Gröcke et al. (2003) who found phosphate (PO_4^{3-}) of presumed

488   biogenic origin being preferentially enriched along concentric growth rings. Generally, the phosphate

489   concentration of ancient belemnite rostra is variable but very low (less than 0.3%) comparable to

490   that in modern *Sepia*.

491   The primary filigree belemnite framework does not fluoresce under the CLFM. The factors

492   that cause fluorescence in samples studied under the CLFM are poorly constrained (Fig. 8). Naturally-

493   occurring organic compounds such as proteins or polysaccharides can cause fluorescence in other

494   biogenic carbonates, including brachiopods (Pérez-Huerta et al., 2008), gastropods (Guzman et al.,

495   2007), or cephalopods (Linzmeier et al., 2016). In modern brachiopods and *Nautilus*, portions of the

496   exoskeletons with higher amounts of intracrystalline organic matter (Clark, 1999) appear dark under

497   CLFM (Pérez-Huerta et al., 2008; Linzmeier et al., 2016). This pattern lends support to the argument

498   that dark triangular areas in BSE images represent the primary biogenic skeleton and contain

499   remnants of organic matter. Marine sediments may contain abundant humic substances resulting

500   from the degradation of marine organic matter (Nissenbaum and Kaplan, 1972) and evidence has

501   been presented that the sulphur content of the humic substances increases with degradation

502   (Francois 1987). Concluding, it is here proposed that humic substances caused elevated S

503   concentrations in the diagenetic calcite phase that occludes the skeletal pore space (Fig. 6D) and

504   causes the CLFM fluorescence in all three wavelengths (Blyth et al., 2008; Orland et al., 2009, 2012;

505   Fig. 8).

506   Similarly, microtomographic data indicate the former presence of organic matter in dark

507   triangular areas of rostra (Fig. 9) as observed in BSE images. The brightness of a carbonate observed

508   in CT image indicates the degree of attenuation of an X-ray passing through this material (Mobilio et

509   al., 2015). As the inner tri-radial structures of rostra appear darker in colour relative to the calcite

510   phase fringing these structures, we suggest that the fringing phase is made of a denser calcite phase

511   compared to the inner structure. That observation is in line with the observation of a low optical

512   relief of these features (supplement Fig. 1A-B).

513   The interpretation presented here with regard to belemnite rostra is arguably consistent with

514   observations of 10-40% organic matrix in the *Sepia* cuttlebone (Birchall and Thomas, 1983; Florek et

515   al., 2009). This is relevant as we suggest that the belemnite rostrum is structurally similar but not

516   homologous (Fuchs 2012) to the *Sepia* cuttlebone with regard to the primary intra-skeletal porosity.

517   Having said this, the presence of preserved organic matter in ancient biogenic carbonates

518   particularly, intra-crystalline organic matter is not uncommon (Clark, 1999, 2005). Excess carbon

519   observed for *Megateuthis* has been interpreted as evidence for a former organic matrix within these

520   low-Mg calcite biominerals (Dunca et al., 2006). Similarly, Florek (2004) argued for an excess of

521   carbon in the rostra of *Belemnopsis* and *Hibolites*. Summing up: Different lines of circumstantial

522   evidence point to the presence of remnant organic matter within biominerals. These data require

523   verification or rejection via the application of spatially highly resolved geochemical data. This work is

524   presently in progress.

525

526   **5. Conclusions**

527   Ultrastructural data documented here suggest that the calcitic rostra of Mesozoic belemnites

528   yielded 50-90% primary porosity probably filled with body fluids and/or organic matter during the life

529   time of the animal. Porosity was distributed throughout the rostrum as opposed to being limited to

530   the central apical area. The primary biogenic rostrum framework consists of triaxial branches and

531   tetrahedrons of variable size forming a honeycomb-like network. This structure arguably combined

532   mechanical stability with an energy-efficient biomineralization strategy.

533   The recognition of belemnite rostra as a highly porous structure requires a re-interpretation of

534   the function of the rostrum as counterweight to the soft body and has implications for the swimming

535   mode of belemnites. On the level of a working hypothesis, we argue that the low-porosity fabric

536   found in fossil rostra collected in outcrops worldwide is the result of a syntaxial, early diagenetic

537   cement phase that nucleated upon the surface of the biogenic framework and subsequently

538   occluded the pore space. The possibility of gradual occlusion of skeletal porosity by remote

539 biomineralization during later ontogenetic stages during the life of the animal is possible but seems

540 unlikely at present.

541   If the here-presented concepts hold true, then these new findings have significant implications

542 with regard to geochemical proxy data collected from fossil belemnite rostra. Specifically, the fact

543 that rostra may consist of biogenic and abiogenic calcite phases formed at different times may

544 explain the controversially low reconstructed seawater temperatures and the uncommonly high

545 scatter of proxy data even from well-preserved rostra collected in the same stratigraphic interval.

546 This is because seawater properties of surficial water masses, the habitat of nektobenthic

547 belemnites, are recorded in the biogenic portions of the rostrum whereas the early diagenetic phase

548 reflects cooler basinal bottom or marine pore water signatures. Findings presented here form a solid

549 and well-constrained petrographic data set but one that must be verified by high-resolution

550 geochemical data of all paragenetic calcite phases observed.

551

552

553   **6. Acknowledgement**

559

560   **7. References**

561 Anderson, T.F., Popp, B.N., Williams, A.C., Ho, L.Z., Hudson, J.D., 1994. The stable isotopic records of

562   fossils from the Peterborough Member, Oxford Clay Formation (Jurassic), UK:

563   palaeoenvironmental implications. Journal of the Geological Society, London 151, 125-138.

564   Arkhipkin, A., Weis, R., Mariotti, N., Shcherbich, Z., 2015. "Tailed" Cephalopods. Journal of Molluscan

565   Studies 81, 345-355.

566   Barbin, V., 1991. Fluctuation in shell composition in *Nautilus* (Cephalopoda, Mollusca): evidence from

567   Cathodoluminescence. Lethaia 25, 391-400.

568   Barbin, V., 2013. Application of cathodoluminescence microscopy to recent and past biological

569   materials: a decade of progress. Mineralogy and Petrology 107, 353-362.

570   Benito, M.I., Reolid, M., 2012. Belemnite taphonomy (Upper Jurassic, Western Tethys) part II: Fossil-

571   diagenetic analysis including combined petrographic and geochemical techniques.

572   Palaeogeography, Palaeoclimatology, Palaeoecology 358, 89-108.

573   Berner, R.A., Westrich, J.T., Graber, R., Smith, J., Martens, C.S., 1978. Inhibition of aragonite

574   precipitation from supersaturated seawater: a laboratory and field study. American Journal of

575   Science 278, 816-837.

576   Birchall, J.D., Thomas, N.L., 1983. On the architecture and function of cuttlefish bone. Journal of

577   Materials Science 18, 2081-2086.

578   Bizikov, V.A., Arkhipkin, A.I., 1997. Morphology and microstructure of the gladius and statolith from

579   the boreal Pacific giant squid *Moroteuthis robusta* (Oegopsida; Onychoteuthidae). Journal of

580   Zoology 241, 475-492.

581   Blyth, A.J., Baker, A., Collins, M.J., Penkman, K.E.H., Gilmour, M.A., Moss, J.S., 2008. Molecular

582   organic matter in speleothems and its potential as an environmental proxy. Quaternary Science

583   Reviews 27, 905–921.

584   Chateigner, D., Hedegaard, C., Wenk, H.R., 2000. Mollusc shell microstructures and crystallographic

585   textures. Journal of Structural Geology 22, 1723-1735.

586   Chinzei, K., Seilacher, A., 1993. Remote Biomineralization I: Fill skeletons in vesicular oyster shells.

587   Neues Jahrbuch für Geologie und Paläontologie, Abhandlungen 190, 349-361.

588   Clark, II G.R., 1999. Organic matrix taphonomy in some molluscan shell microstructures.

589   Palaeogeography, Palaeoclimatology, Palaeoecology 149, 305-312.

590   Clark, II G.R., 2005. Organic matrix in the porifera and Cnidaria: déjà vu through a temporal

591   telescope. Geological society of America Abstracts with Program 37, 366.

592   Cochran, J.K., Landman, N.H., Turekian, K.K., Michard, A., Schrag, D.P., 2003. Paleoceanography of

593   the Late Cretaceous (Maastrichtian) Western Interior Seaway of North America: evidence from Sr

594   and O isotopes. Palaeogeography Palaeoclimatology Palaeoecology 191, 45-64.

595   Cochran, J.K., Kallenberg, K., Landman, N.H., Weinreb, D., Turekian, K.K., Beck, A.J., Cobban, W.A.,

596   2010. Effect of diagenesis on the Sr, O, and C isotope composition of Late Cretaceous Mollusks

597   from the Western Interior Seaway of North America. American Journal of Science 310, 69-88.

598   Coronado, I., Pérez-Huerta, A., Rodríguez, S., 2013. Primary biogenic skeletal structures in

599   Multithecopora (Tabulata, Pennsylvanian). Palaeogeography, Palaeoclimatology, Palaeoecology

600   386, 286-299.

601   Dunca, E., Doguzhaeva, L., Schöne, B.R., Schootbrugge, B. v.d., 2006. Growth patterns in rostra of the

602   Middle Jurassic belemnite *Megateuthis giganteus*: controlled by the moon? Acta Universitatis

603   Carolinae – Geologica 49, 107-117.

604   Dupraz, C., Reid, R.P., Braissant, O., Decho, A.W., Norman, R.S., Visscher, P.T., 2009. Processes of

605   carbonate precipitation in modern microbial mats. Earth-Science Reviews 96, 141-162.

606   Dutton, A., Huber, B.T., Lohmann, K.C., Zinsmeister, W.J., 2007. High-Resolution Stable Isotope

607   Profiles of a Dimitobelid Belemnite: Implications for Paleodepth Habitat and Late Maastrichtian

608   Climate Seasonality. Palaios 22, 642–650.

609   Florek, M., Youn, H.S., Ro, C.U., Wierzbowski, H., Osán, J., Kazimierczak, W., Kuczumow, A., 2004.

610   Investigation of chemical composition of belemnite rostra by synchrotron-based X-ray

611   microfluorescence and diffraction and electron microprobe. Journal of Alloys and Compounds

612   362, 99-106.

613   Florek, M., Fornal, E., Gomez-Romero, P., Zieba, E., Paszkowicz, W., Lekki, J., Nowak, J., Kuczumow,

614   A., 2009. Complementary microstructural and chemical analyses of *Sepia officinalis*

615   endoskeleton. Materials Science and Engineering C 29, 1220-1226.

616   Francois, R., 1987. A study of sulphur enrichment in the humic fraction of marine sediments during

617   early diagenesis. Geochimica et Cosmochimica Acta 51, 17–27.

618   Fuchs, D., 2012. The "rostrum"-problem in coleoid terminology – an attempt to clarify

619   inconsistencies. Geobios 45, 29-39.

620   Goetz, A.J., Steinmetz, D.R., Griesshaber, E., Zaefferer, S., Raabe, D., Kelm, K., Irsen, S., Sehrbrock, A.,

621   Schmahl, W.W., 2011. Interdigitating biocalcite dendrites from a 3-D jigsaw structure in

622   brachiopod shells. Acta Biomaterialia 7, 2237-2243.

623   Gröcke, D.R., Price, G.D., Ruffell, A.H., Mutterlose, J., Baraboschkin, E., 2003. Isotopic evidence for

624   Late Jurassic-Early Cretaceous climate change. Palaeogeography, Palaeoclimatology,

625   Palaeoecology 202, 97-118.

626   Guerra, A., 2006. Ecology of *Sepia officinalis*. Vie et Milieu – Life & Environment 56, 97-107.

627   Guzman, N., Ball, A.D., Cuif, J.-P., Dauphin, Y., Denis, A., Ortlieb, L., 2007. Subdaily growth patterns

628   and organo-mineral nanostructure of the growth layers in the calcitic prisms of the shell of

629   *Concholepas concholepas* Bruguière, 1789 (Gastropoda, Muricidae). Microscopy and

630   Microanalysis 13, 397-403.

631   Huber, B.T., Hodell, D.A., 1996. Middle-Late Cretaceous climate of the Southern high latitudes: Stable

632   isotopic evidence for minimal equator-to-pole thermal gradients: Discussion and reply.

633   Geological Society of America Bulletin 108, 1193-1196.

634   Hückel, U., Hemleben, C., 1976. Diagenetische Spurenelement-Verschiebungen und Veränderungen

635   der Skelett-Strukturen bei Belemniten Rostren. Zentralblatt Geologie und Paläontologie Teil II

636   1976, 362-365.

637   Immenhauser, A., Schöne, B.R., Hoffmann, R., Niedermayr, A., 2016. Mollusc and brachiopod skeletal

638   hard parts: Intricate archives of their marine environment. Sedimentology 63, 1-59.

639   Jarvis, I., Trabucho-Alexandre, J., Gröcke, D., Uličný, D., Laurin, J., 2015. Intercontinental correlation

640   of organic carbon and carbonate stable isotope records: evidence of climate and sea-level change

641   during the Turonian (Cretaceous). The Depositional Record 1, 53-90.

642   Klug, C., Schweigert, G., Fuchs, D., Kruta, I., Tischlinger, H., 2015. Adaptations to squid-style high-

643   speed swimming in Jurassic belemnitids. Biological Letters 12, 1-5.

644   Kozdon, R., Kelly, D.C., Kita, N.T., Fournelle, J.H., Valley, J.W., 2011. Planktonic foraminiferal oxygen

645   isotope analysis by ion microprobe technique suggests warm tropical sea surface temperatures

646   during the Early Paleogene. Paleoceanography 26, 1-17.

647   Li, Q., 2011. Belemnite Palaeo-proxies and Dating of Mesozoic Carbonates. Ph.D. Thesis. 1-262,

648   Department of Earth Sciences, Univeristy College London.

649   Li, Q., McArthur, J.M., Atkinson, T.C., 2012. Lower Jurassic belemnites as indicators of palaeo-

650   temperature. Palaeogeography Palaeoclimatology, Palaeoecology 315, 38-45.

651   Li, Q., McArthur, J.M., Doyle, P., Janssen, N., Leng, M.J., Müller, W., Reboulet, S., 2013. Evaluating

652   Mg/Ca in belemnite calcite as a palaeo-proxy. Palaeogeography Palaeoclimatology,

653   Palaeoecology 388, 98-108.

654   Linzmeier, B.J., Kozdon, R., Peters, S.E., Valley, J.W., 2016. Oxygen isotope variability within *Nautilus*

655   shell growth bands. PLoS ONE (Accepted).

656   Longinelli, A., Iacumin, P., Ramigni, M., 2002. $\delta^{18}O$ of carbonate, quartz and phosphate from

657   belemnite guards: implications for the isotopic record of old fossils and the isotopic composition

658   of ancient seawater. Earth and Planetary Science Letters 203, 445-459.

659   Longinelli, A., Wierzbowski, H., Matteo, A. di, 2003. $\delta^{18}O(PO_4^{3-})$ and $\delta^{18}O(CO32-)$ from belemnite

660   guards from Eastern Europe: implications for palaeoceanographic reconstructions and for the

661   preservation of pristine isotopic values. Earth and Planetary Science Letters 209, 337-350.

662   Lowenstam, H.A., Weiner, S., 1989. On Biomineralization. Oxford University Press, New York 324 pp.

663   Lukeneder, A., Harzhauser, M., Müllegger, S., Piller, W.E., 2010. Ontogeny and habitat change in

664   Mesozoic cephalopods revealed by stable isotopes ($\delta^{18}O$, $\delta^{13}C$). Earth and Planetary Science

665   Letters 296, 103-114.

666 Massonne, H.-J., Neuser, R.D., 2005. Ilmenite exsolution in olivine from the serpentinite body at

667   Zöblitz, Saxonian Erzgebirge – microstructural evidence using EBSD. Mineralogical Magazine 69,

668   119-124.

669 McArthur, J.M., Janssen, N.M.M., Reboulet, S., Leng, M.J., Thirlwall, M.F., Schootbrugge, B. v.d.,

670   2007. Palaeotemperatures, polar ice-volume, and isotope stratigraphy (Mg/Ca, δ^{18}O, δ^{13}C,

671   ^{87}Sr/^{86}Sr): The Early Cretaceous (Berriasian, Valanginian, Hauterivian). Palaeogeography

672   Palaeoclimatology, Palaeoecology 248, 391-430.

673 Mobilio, S., Boscherini, F., Meneghini, C., 2015. Synchrotron Radiation: Basics, Methods and

674   Applications. Springer Berlin Heidelberg.

675 Mokso, R., Marone, F., Irvine, S., Nyvlt, M., Schwyn, D., Mader, K., Taylor, G.K., Krapp, H.G., Skeren,

676   M., Stampanoni, M., 2013. Advantages of phase retrieval for fast X-ray tomographic microscopy.

677   Journal of Physics D: Applied Physics 46, 1-12.

678 Müller-Stoll, H., 1936. Beiträge zur Anatomie der Belemnoidea. Nova Acta Leopoldina-Abhandlungen

679   der Kaiserlich Leopoldinisch-Carolinisch Deutschen Akademie der Naturforscher, Neue Folge 4, 1-

680   70.

681 Neuser, R.D., Bruhn, F., Götze, J., Habermann, D., Richter, D.K., 1996. Kathodolumineszenz: Methodik

682   und Anwendung. Zentralblatt Geologie und Paläontologie Teil 1 1995, 287-306.

683 Niebuhr, B., 1995. Fazies-Differenzierungen und ihre Steuerungsfaktoren in der höheren Oberkreide

684   von   S-Niedersachsen/Sachsen-Anhalt   (N-Deutschland).   Berliner   Geowissenschaftliche

685   Abhandlungen, Reihe A 174, 1-131.

686 Niebuhr, B., Hiss, M., Kaplan, U., Tröger, K.A., Voigt, S., Voigt, T., Wiese, F., Wilmsen, M., 2007.

687   Lithostratigraphie der norddeutschen Oberkreide. Schriftenreihe der Deutschen Gesellschaft für

688   Geowissenschaften 55, 1-136.

689 Nissenbaum, A., Kaplan, I.R., 1972. Chemical and isotopic evidence for the *in situ* origin of marine

690   humic substances. Limnology and Oceanography 17, 570-582.

691   Orland, I.J., Bar-Matthews, M., Kita, N.T., Ayalon, A., Matthews, A., & Valley, J.W., 2009. Climate

692   deterioration in the Eastern Mediterranean as revealed by ion microprobe analysis of a

693   speleothem that grew from 2.2 to 0.9 ka in Soreq Cave, Israel. Quaternary Research 71, 27–35.

694   Orland, I.J., Bar-Matthews, M., Ayalon, A., Matthews, A., Kozdon, R., Ushikubo, T., Valley, J.W., 2012.

695   Seasonal resolution of Eastern Mediterranean climate change since 34 ka from a Soreq Cave

696   speleothem. Geochimica et Cosmochimica Acta 89, 240–255.

697   Oti, M.N., Ogbuji, L.U., Breuer, K.H., 1989. Diagenetic transformation of magnesium calcite in a

698   monocrystalline rock-forming carbonate skeleton of an echinoderm. Chemical Geology 76, 303-

699   308.

700   Parkinson, D., Curry, G.B., Cusack, M., Fallick, A.E., 2005. Shell structure, patterns and trends of

701   oxygen and carbon stable isotopes in modern brachiopod shells. Chemical Geology 219, 193-235.

702   Podlaha, O.G., Mutterlose, J., Veizer, J., 1998. Preservation of $\delta^{18}O$ and $\delta^{13}C$ in belemnite rostra from

703   the Jurassic/Early Cretaceous successions. American Journal of Science 298, 324-347.

704   Price, G.D., Page, K.N., 2008. A carbon and oxygen isotopic analysis of molluscan faunas from the

705   Callovian-Oxfordian boundary at Redcliff Point, Weymouth, Dorset: implications for belemnite

706   behaviour. Proceedings of the Geologists´ Association 119, 153-160.

707   Price, G.D., Sellwood, B.W., 1997. "Warm" palaeotemperatures fron high Late Jurassic

708   palaeolatitudes (Falkland Plateau): Ecological, environmental or diagenetic controls?

709   Palaeogeography Palaeoclimatology, Palaeoecology 129, 315-327.

710   Price, G.D., Wilkinson, D., Hart, M.B., Page, K.N., Grimes, S.T., 2009. Isotopic analysis of coexisting

711   Late Jurassic fish otoliths and molluscs: Implications for upper-ocean water temperature

712   estimates. Geology 37, 215-218.

713   Price, G.D., Fözy, I., Janssen, N.M.M., Pálfy, J., 2011. Late Valanginian-Barremian (Early Cretaceous)

714   palaeotemperatures inferred from belemnite stable isotope and Mg/Ca ratios from Bersek

715   Quarry (Gerecse Mountains, Trandanubian Range, Hungary). Palaeogeography

716   Palaeoclimatology, Palaeoecology 305, 1-9.

717   Price, G.D., Hart, M.B., Wilby, P.R., Page, K.N., 2015. Isotopic analysis of Jurassic (Callovian) molluscs

718   from the Christian Malford Lagerstätte (UK): Implications for ocean water temperature estimates

719   based on belemnoids. Palaios 30, 645-654.

720   Richter, D.K., Götte, T., Götze, J., Neuser, R.D., 2003. Progress in application of cathodoluminescence

721   (CL) in sedimentary petrology. Mineralogy and Petrology 79, 127-166.

722   Richter, D.K., Neuser, R.D., Schreuer, J., Gies, H., Immenhauser, A., 2011. Radiaxial-fibrous calcites: a

723   new look on an old problem. Sedimentary Geology 239, 23-36.

724   Ritter, A.-C., Kluge, T., Berndt, J., Richter, D.K., John, C.M., Bodin, S., Immenhauser, A., 2015.

725   Application of redox sensitive proxies and carbonate clumped isotopes to Mesozoic and

726   Palaeozoic radiaxial fibrous cements. Chemical Geology 417, 306-321.

727   Ritter, A.-C., Mavromatis, V., Dietzel, M., Wiethoff, F., Griesshaber, E., Casella, L., Schmahl, W.,

728   Koelen, J., Neuser, R.D., Leis, A., Buhl, D., Niedermayr, A., Bernasconi, S.M., Immenhauser, A.

729   (submitted). Experimental diagenesis: I – Exploring the impact of diagenesis on (isotope)

730   geochemical and microstructural features in biogenic aragonite. Geochimica et Cosmochimica

731   Acta.

732   Rosales, I., Quesada, S., Robles, S., 2001. Primary and diagenetic isotopic signals in fossils and

733   hemipelagic carbonates: the Lower Jurassic of northern Spain. Sedimentology 48, 1149-1169.

734   Rosales, I., Quesada, S., Robles, S., 2004a. Paleotemperature variations of Early Jurassic seawater

735   recorded in geochemical trends of belemnites from the Basque-Cantabrian basin, northern Spain.

736   Palaeogeography, Palaeoclimatology, Palaeoecology 203, 253-275.

737   Rosales, I., Robles, S., Quesada, S., 2004b. Elemental and oxygen isotope composition of Early

738   Jurassic Belemnites: Salinity vs. Temperature signals. Journal of Sedimentary Research 74, 342-

739   354.

740   Saelen, G., 1989. Diagenesis and construction of the belemnite rostrum. Palaeontology 32, 765-798.

741   Seilacher, A., Chinzei, K., 1993. Remote Biomineralization 2: Fill skeletons controlling buoyancy in

742   shelled cephalopods. Neues Jahrbuch für Geologie und Paläontologie, Abhandlungen 190, 363-

743   373.

744   Sessa, J.A., Larina, E., Knoll, K., Garb, M., Cochran, J.K., Huber, B.T., MacLeod, K.G., Landman, N.H.,

745   2015. Ammonite habitat revealed via isotopic composition and comparisons with co-occurring

746   benthic and planktonic organisms. Proceedings of the National Academy of Sciences of the

747   United States of America 112, 15562-15567.

748   Sherrard, K.M., 2000. Cuttlebone Morphology Limits Habitat Depth in Eleven Species of *Sepia*

749   (Cephalopoda: Sepiidae). Biological Bulletin 198, 404-414.

750   Spaeth, C., 1971. Aragonitische und calcitische Primärstrukturen im Schalenbau eines Belemniten aus

751   der englischen Unterkreide. Paläontologische Zeitschrift 45, 33-40.

752   Spaeth, C., 1973. Weitere Untersuchungen der Primär- und Fremdstrukturen in calcitischen und

753   aragonitischen Schalenlagen englischer Unterkreide-Belemniten. Paläontologische Zeitschrift 47,

754   163-174

755   Spaeth, C., 1975. Zur Frage der Schwimmverhältnisse bei Belemniten in Abhängigkeit vom

756   Primärgefüge der Hartteile. Paläontologische Zeitschrift 49, 321-331.

757   Stevens, G.R., 1965. The Jurassic and Cretaceous Belemnites of New Zealand and a Review of the

758   Jurassic and Cretaceous Belemnites of the Indo-Pacific Region. New Zealand Geological Survey

759   Paleontological Bulletin 36, 1-283.

760   Swart, P.K., 2015. The geochemistry of carbonate diagenesis: The past, present and future.

761   Sedimentology 62, 1233-1304.

762   Ullmann, C.V., Korte, C., 2015. Diagenetic alteration in low-Mg calcite from macrofossils: A review.

763   Geological Quarterly 59, 3-20.

764   Ullmann, C.V., Frei, R., Korte, C., Hesselbo, S.P., 2015. Chemical and isotopic architecture of the

765   belemnite rostrum. Geochemica et Cosmochimica Acta 159, 231-243.

766   Ullmann, C.V., Thibault, N., Ruhl, M., Hesselbo, S.P., Korte, C., 2014. Effect of a Jurassic oceanic

767   anoxic event on belemnite ecology and evolution. Proceedings of the National Academy of

768   Sciences of the United States of America 111, 10073-10076.

769   Urey, H.C., Lowenstein, H.A., Epstein, S., McKinney, C.R., 1951. Measurements of paleotemperatures

770   and temperatures of the upper Cretaceous of England, Denmark, and the southern United States.

771   Bulletin of the Geological Society of America 62, 399-416.

772   Veizer, J., 1974. Chemical diagenesis of belemnite shells and possible consequences for

773   paleotemperature determination. Neues Jahrbuch für Geologie und Paläontologie,

774   Abhandlungen 147: 91-111.

775   Visscher, P.T., Stolz, J.F., 2005. Microbial mats as bioreactors: populations, processes and products.

776   Palaeogeography, Palaeoclimatology, Palaeoecology 219, 87-100.

777   Voigt, S., Wilmsen, M., Mortimore, R.N., Voigt, T., 2003. Cenomanian palaeotemperatures derived

778   from the oxygen isotopic composition of brachiopods and belemnites: evaluation of Cretaceous

779   palaeotemperature proxies. International Journal of Earth Sciences (Geologische Rundschau) 92,

780   285-299.

781   Wanamaker, A.D., Baker, A., Butler, P.G., Richardson, C.A., Scourse, J.D., Ridgway, I., Reynolds, D.J.,

782   2009. A novel method for imaging internal growth patterns in marine mollusks: A fluorescence

783   case study on the aragonitic shell of the marine bivalve *Arctica islandica* (Linnaeus). Limnology

784   and Oceanography: Methods 7, 673-681.

785   Weiner, S., Addadi, L., 2011. Crystalization Pathways in Biomineralization. Annual Review of Materials

786   Research 41, 21-40.

787   Wierzbowski, H., 2004. Carbon and oxygen isotope composition of Oxfordian-Early Kimmeridgian

788   belemnite rostra: palaeoenvironmental implications for Late Jurassic seas. Palaeogeography,

789   Palaeoclimatology, Palaeoecology 203, 153-168.

790 Wierzbowski, H., Joachimski, M.M., 2007. Reconstruction of late Bajocian-Bathonian marine

791   palaeoenvironments using carbon and oxygen isotope ratios of calcareous fossils from the Polish

792   Jura chain (central Poland). Palaeogeography, Palaeoclimatology, Palaeoecology 254, 523-540.

793 Wierzbowski, H., Joachimski, M.M., 2009. Stable Isotopes, Elemental Distribution, and Growth Rings

794   of Belemnopsid Belemnite Rostra: Proxies for Belemnite Life Habitat. Palaios 24, 377-386.

795 Zachos, J., Pagani, M., Sloan, L., Thomas, E., Billups, K., 2001. Trends, Rhythms, and aberrations

796   inglobal climate 65 Ma to present. Science 292, 686-693.

797

798

799

800

801

802

803 **Figure captions**

804

805 **Fig. 1A-B) Structural and ultrastructural composition of belemnite rostra.** *Belemnitella mucronata*,

806 thin sections photographed under crossed polarizers. A) Cross section with pseudo-uniaxial cross

807 indicating radially arranged calcite fibres, red box refers to C. B) Longitudinal section with central

808 apical line and radiating fibres from the centre to the margin, stippled line refers to the position of

809 cross section shown in A. C) Idealized bundle of calcite fibres, each fibre contains a stack of

810 tetrahedral elements. D) SEM BSD image of the tetrahedral ultrastructure of *Megateuthis gigantea*,

811 dashed lines (I-IV) indicate section planes and corresponding reconstructions. Primary skeletal

812 framework is shown in blue, yellow and green whilst early diagenetic phase is shown in white and

813 red for the crystal boundaries. The basis of tetrahedrons points toward the centre of the belemnite

814 rostrum and its tip towards the rostrum margin i.e. the growth direction. E) Three dimensional

815   reconstruction of a single tetrahedron of the belemnite endoskeleton. F) Reconstruction of the

816   complex spatial arrangement of biogenic and early diagenetic phases. Colour code in lower right. G)

817   SEM image of a single complex tetrahedron (black line) with indication of structural elements.

818   Primary skeletal components: br = branch, trc = triradial centre, rf = reinforcement, ic = isopachous

819   crystallites. **(full page width; bw in print, colour in pdf)**

820

821   **Fig. 2A-B) SEM BSD images of *Megateuthis gigantea*.** A-B) Section perpendicular to the c-axes of

822   calcite fibres (section plane II in Fig. 1D-II). White stippled line indicate dissolution features (early

823   diagenetic), black stippled line indicate microstylolites. **(full page width; bw in print, colour in pdf)**

824

825   **Fig. 2A-B) SEM BSD images of *Megateuthis gigantea*.** A-B) Section perpendicular to the c-axes of

826   calcite fibres (section plane II in Fig. 1D-II). Blue stippled line indicate dissolution features (early

827   diagenetic), red stippled line indicate microstylolites. **(full page width; bw in print, colour in pdf)**

828

829

830   **Fig. 3A-F) SEM BSD images of *Megateuthis gigantea*.** A-E) Section perpendicular to the c-axes of

831   calcite fibres. A) Triangular structures with a relatively thick outer, light grey margin of abiogenic

832   early diagenetic cement and a small darker centre with branches giving rise to reinforcement

833   structures representing the primary biogenic skeletal framework. B) Larger dark grey, organic rich

834   triangular elements belonging to the biogenic skeletal framework, partly with light grey central

835   abiogenic calcite filling of variable sizes. Branches are often short and cut off at variable distances

836   from the centre. C) Some smaller and a few larger biogenic skeletal elements with cut off branches

837   (lower arrow) and reinforcement structures (upper arrow). Note the variable expression of early

838   diagenetic crystallites with sheaths of remnant organic matter. D) Close up of larger, biogenic skeletal

839   elements and abiogenic isopachous calcites coated by remnants of organic matter within the brighter

840   outer margin. Central portion of the biogenic skeletal elements shows abiogenic crystal; arrows point

841   to dissolved branches. E) Centre of biogenic skeletal element completely filled with abiogenic bright

842   calcite leaving only a thin dark inner margin. F) Same specimen, section subparallel to the c-axes

843   showing a homogenous central portion ("trunk" – white line) of pyramidal morphology rich in

844   intracrystalline organic matter surrounded by inclined isopachous calcite crystals coated by remnants

845   of organic matter. This overall pattern results in a "Christmas tree like" structure (compare with Fig.

846   1D). **(full page width; bw in print and pdf)**

847

848   **Fig. 4A-E)** *Megateuthis gigantea*, EBSD map with colour code in sections perpendicular to the c-axes

849   of the fiber bundles. Same colours represent same crystallographic orientations. In A and B angular

850   deviation from blue to red is up to 40°, in D angular deviation is 2°. A) Overview map showing the

851   bundling of fibres with identical orientation of a-axes, black frame indicates area for close up in B;

852   blue frame refers to Fig. 5A-C. B) Close up map, within one bundle blue tinted fibres are mainly

853   neighboured by other blue fibres, red tinted fibres are surrounded by red fibres. C) Close up

854   documenting minor angular deviation within one fibre (compare with D). D) Map of a single fibre

855   with an angular deviation of 2° from blue to red, showing a slight systematic shift of axes orientation.

856   E) Pole-plots of c-axes {001} and a-axes {010} from all fibres shown in A, all c-axes show nearly the

857   same orientation while the a-axes demonstrate the bundled structure of the rostral fabric which may

858   have improved the stability of the skeletal structure. **(full page width; bw in print, colour in pdf)**

859

860

861

862

863

864

865

866

867

868

869

870

871

Fig. 5A-F) Transmitted light, polarized light and cathodoluminescence. Thin section of *Megateuthis gigantea*, A-C refer to the blue frame in Fig. 4A, D-F are close ups (black frame in A) A and D) TL image perpendicular to the c-axes of calcite fibres, filigree biogenic skeletal framework is indicated by the dark tinted structures, primary porosity is represented by the abiogenic translucent calcites. Note banded distribution of calcite fibre domains relating to larger and smaller organic-rich biogenic skeletal elements, single fibres may contain a central portion of transparent calcite of varying size, bundling of adjacent calcite fibres is indicated by the same orientation of the triangles. B and E) Uniform extinction (orientation) of adjacent fibres under crossed polarizers. C and F) CL of abiogenic calcite portions show a dark blue, intrinsic luminescence (pure stoichiometric calcite), CL of the biogenic skeletal framework show light blue luminescence. **(full page width; bw in print, colour in pdf)**

883

884

Fig. 6) Electron microprobe data for *Megateuthis gigantea*. A) Overview BSE map B) Shows higher Mg concentrations within the triangular areas dark in BSE images and a lower Mg concentration in the surrounding area bright in BSE images. C) Shows higher P concentrations within the triangular areas dark in BSE images and a lower P concentration in the surrounding area bright in BSE images. D) Shows lower S concentrations within the triangular areas dark in BSE images and higher S concentrations in the surrounding region bright in BSE images. **(full page width; bw in print, colour in pdf)**

892

893

894

Fig. 7) Fluorescence microscope images for *Megateuthis gigantea*. A) Transmitted light shows brownish triangular structures, rich in organic matter and dark in BSE images, partly with central translucent areas (compare with Fig. 1D section plane IV, Fig. 3D, E, 5A, D). B) Shows brighter fluorescent triangular area compared to the in transmitted light translucent calcite. **(full page width; bw in print, colour in pdf)**

900

901

Fig. 8) Confocal laser fluorescence microscopy images of *Megateuthis gigantea*. A) CLFM images showing fluorescence in far-red light (λ = 664 to 696 nm). B) CLFM images showing fluorescence in visible green light (λ = 505 to 539 nm). C and D) CLFM images showing fluorescence in visible red light (λ = 589 to 621 nm). Triangular structures visible in other imaging techniques (Fig. 3, 5-7) do not fluoresce as brightly as cracks (B) or early diagenetic calcite (Fig. 3) separating the triangles (A, B, C, D). D) Higher magnification shows some brighter fluorescing calcite between the triangular elements dark in BSE images (Fig. 1, 3). Brightly fluorescent early diagenetic calcite separating triangles is enriched in S (Fig. 6). **(full page width; bw in print, colour in pdf)**

910

911

Fig. 9) Three-dimensional visualization of the filigree biogenic framework. Synchrotron radiation based tomographic visualization of a sub-volume of the rostrum of *Megateuthis gigantea*. Specimen was scanned with an isotropic voxel size of 0.74μm. A) Multi-planar image of a sub-domain of the original dataset with dimensions of 447x592x663 voxels, triangular elements dark in BSE images appear here as dark elements due to reduced densities. B-D) Volumetric renderings of the same sub-domain with variable rendering settings. **(full page width; bw in print, colour in pdf)**

918

920   **Supplementary Figures**

921   **Fig. 1) Examples of the filigree framework from other belemnite species.** A-B) *Gonioteuthis*

922   *quadrata*, A) shows the Becke line outside of the triangular area with a relatively larger distance

923   between the sample and objective. B) Image shows the Becke line within the triangular area while

924   the distance between the sample and the objective was reduced, accordingly the triangular area

925   (dark in BSE; Fig. 3) has a lower optical relief. C-D) *Belemnitella mucronata*, C) thin section under

926   polarized light, D) same area under CL showing microfractures filled with Mn-rich calcite tracing the

927   outline of triangular elements (encircled). **(full page width; bw in print, colour in pdf)**

928

929

930   **Fig. 2) SEM BSD images of *Megateuthis gigantea*.** A-F) Section plane parallel to the c-axes of calcite

931   fibres. A-C) stepwise enlargement of a particular area. D-F) stepwise enlargement of a particular

932   area. A and D give the impression of a concentric arrangement of distinct darker and brighter layers

933   (black frames enlarged in B and E), arrow in D point to an organic rich layer (laminae obscura sensu

934   Müller-Stoll, 1936). B and E) Allow the recognition of single darker structures of tetrahedral

935   morphology with their tips pointing towards the outer margin of the belemnite rostrum, i.e. the

936   growth direction (black frames enlarged in C and F). C and F) show the intricate framework of

937   biogenic (dark) and abiogenic (light) carbonate phase within the rostrum, larger dark grey, triangular

938   elements belonging to the biogenic skeletal framework, partly with light grey central abiogenic

939   calcite filling of variable size. **(full page width; bw in print, colour in pdf)**

940

Highlights

We present well-constrained petrographic evidence for the complex primary biogenic framework of belemnite rostra.

Petrographic evidence demonstrates a high (50-90%) primary porosity for the bulk of the belemnite rostrum.

The relative proportion of biogenic skeletal framework versus abiogenic, earliest diagenetic calcite occluding the former pore space in rostra is assessed.

We discuss the timing and formation modes of pore-filling calcites.

The significance of these findings for reconstructions of marine palaeo-environments and the function of the rostrum is discussed.
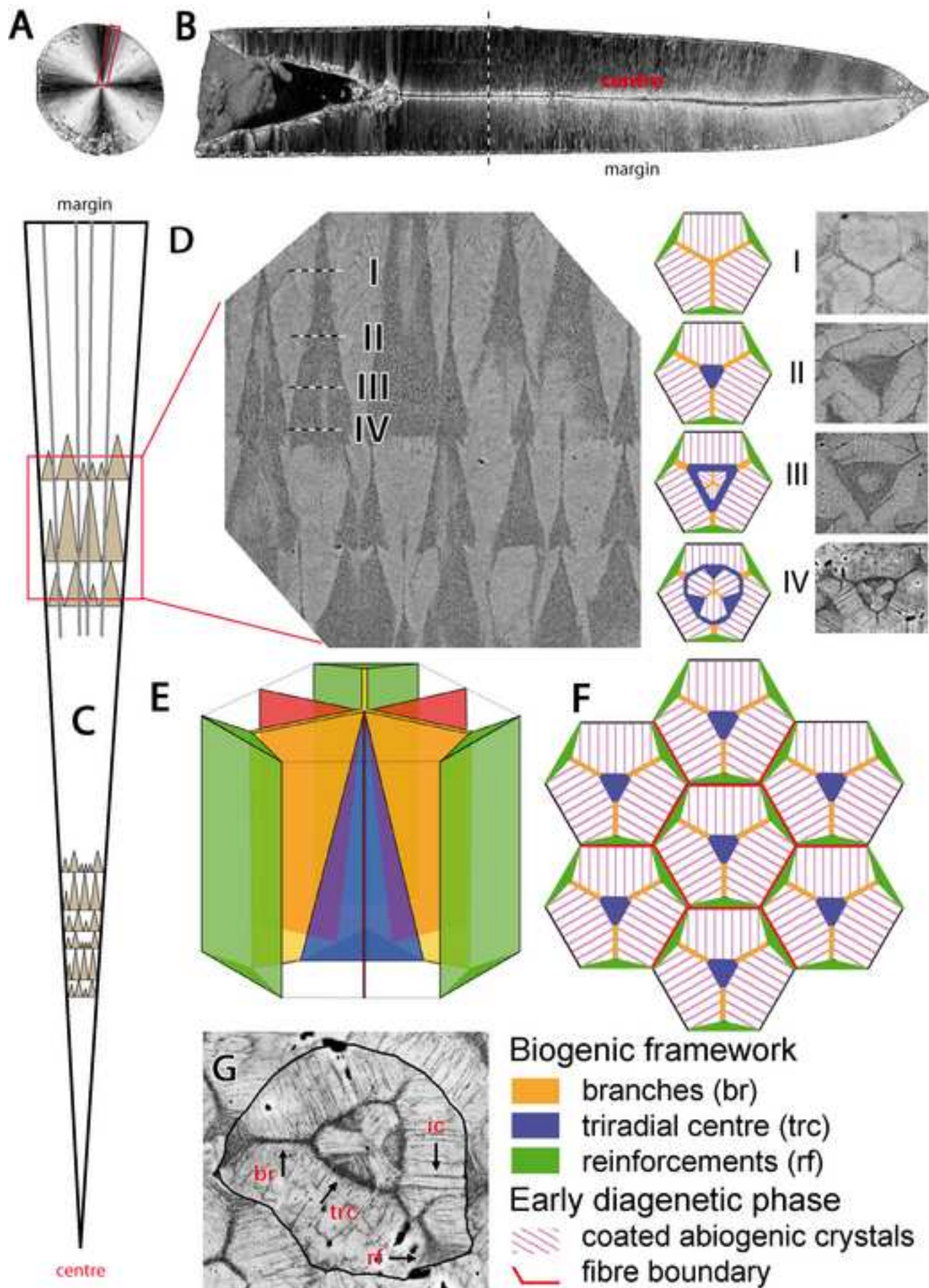
A

B

margin

centre

margin

D

I
II
III
IV

I

II

III

IV

C

E

F

G

ic

br

trc

rf

Biogenic framework

branches (br)

triradial centre (trc)

reinforcements (rf)

Early diagenetic phase

coated abiogenic crystals

fibre boundary

centre

B

200 μm

A

500 μm

C

20 μm

E

D

{001}

y0

x0

{010}

25 μm
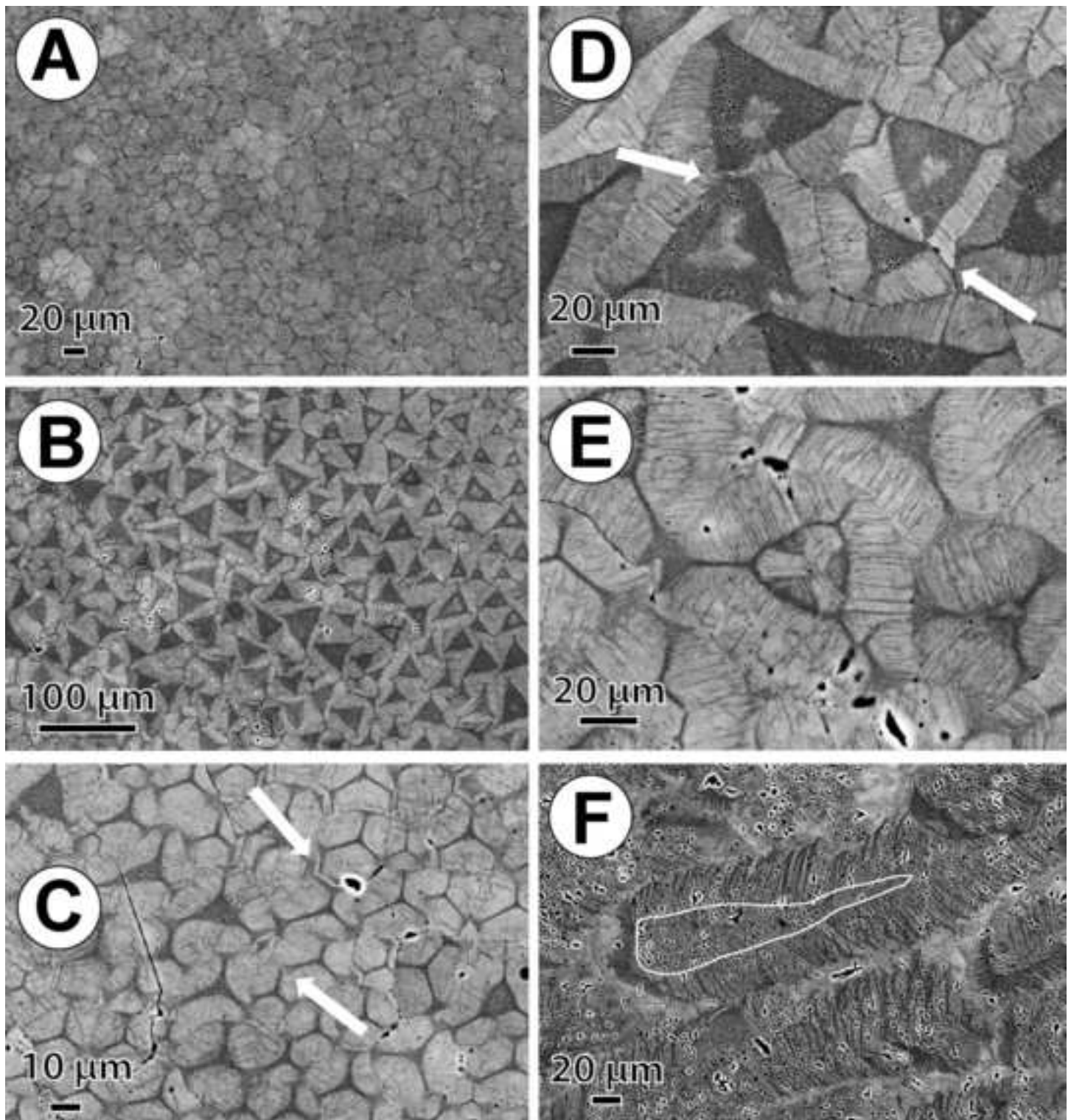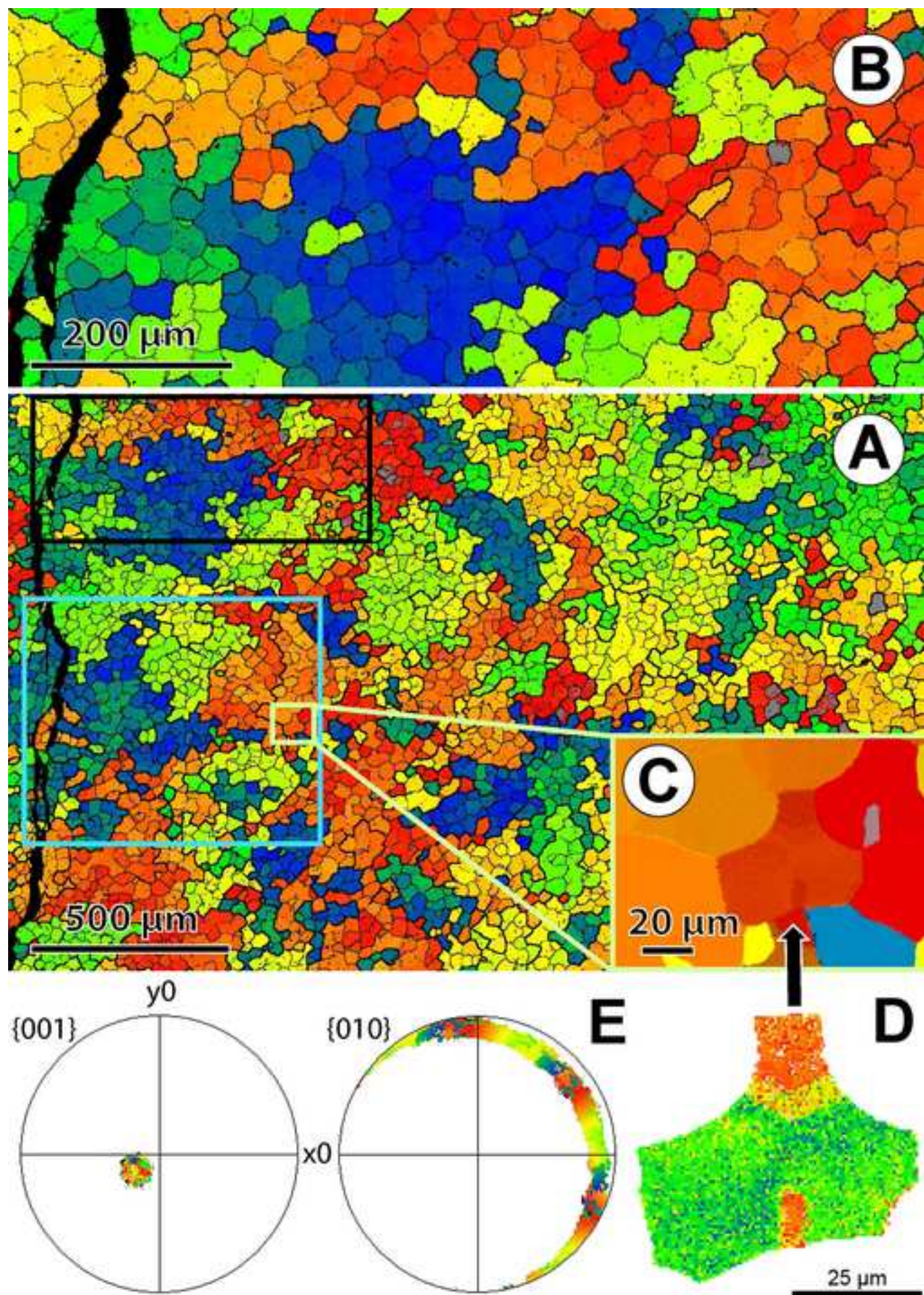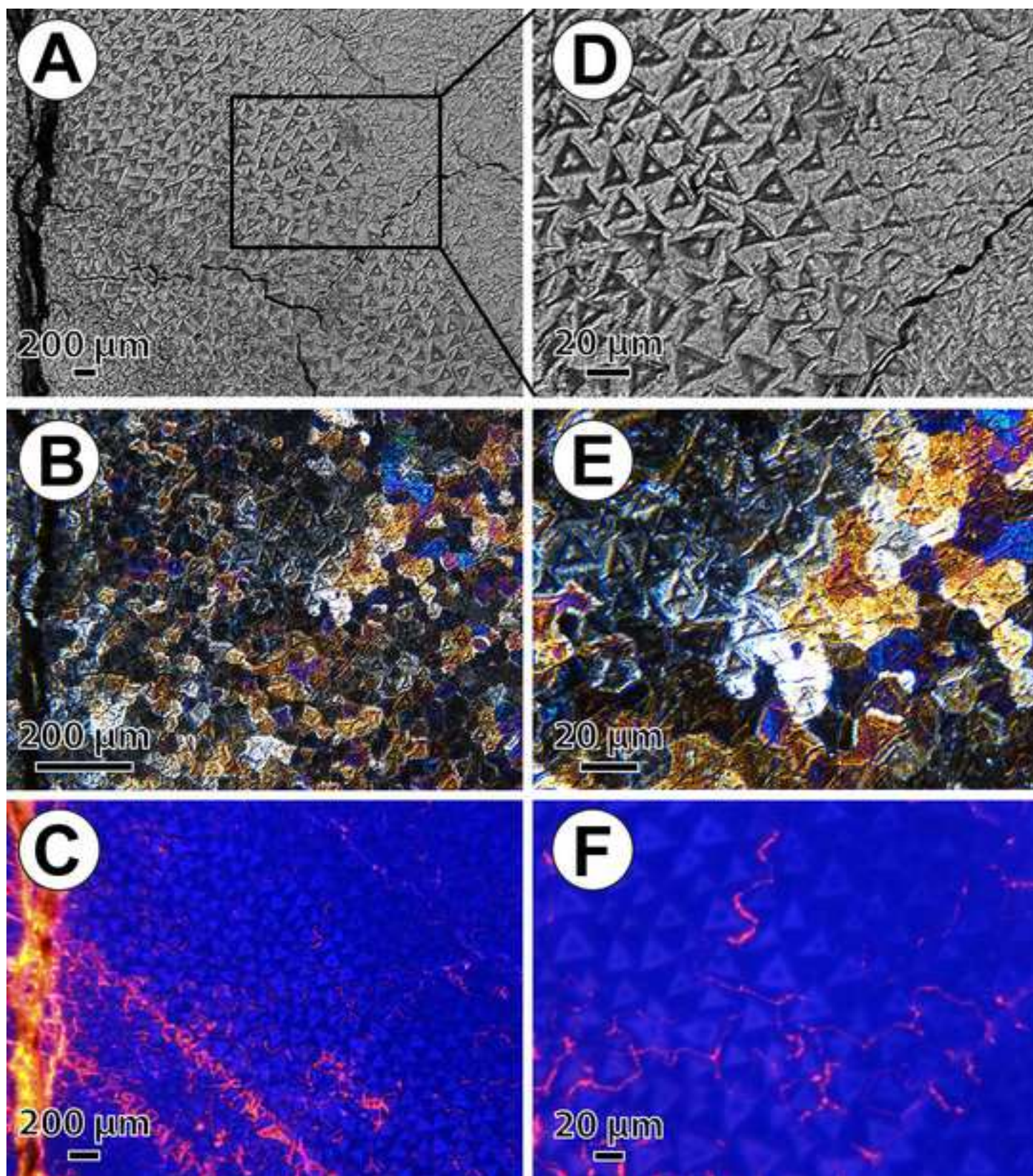
Supplementary material for on-line publication only
Click here to download Supplementary material for on-line publication only: Supplement Fig. 1 - full-width.jpg

Supplementary material for on-line publication only